NASA/TM-20240003659

# Design of an In-Slot Cooled Air-Core Flux-Focusing Permanent Magnet Synchronous Machine for Electric Aircraft Applications

*Jonathan Gutknecht, Thomas Tallerico, and Aaron Anderson*
*Glenn Research Center, Cleveland, Ohio*

May 2024

# NASA STI Program Report Series

Since its founding, NASA has been dedicated to the advancement of aeronautics and space science. The NASA scientific and technical information (STI) program plays a key part in helping NASA maintain this important role.

The NASA STI program operates under the auspices of the Agency Chief Information Officer. It collects, organizes, provides for archiving, and disseminates NASA's STI. The NASA STI program provides access to the NTRS Registered and its public interface, the NASA Technical Reports Server, thus providing one of the largest collections of aeronautical and space science STI in the world. Results are published in both non-NASA channels and by NASA in the NASA STI Report Series, which includes the following report types:

- TECHNICAL PUBLICATION.
  Reports of completed research or a major significant phase of research that present the results of NASA Programs and include extensive data or theoretical analysis. Includes compilations of significant scientific and technical data and information deemed to be of continuing reference value. NASA counterpart of peer-reviewed formal professional papers but has less stringent limitations on manuscript length and extent of graphic presentations.

- TECHNICAL MEMORANDUM.
  Scientific and technical findings that are preliminary or of specialized interest, e.g., quick release reports, working papers, and bibliographies that contain minimal annotation. Does not contain extensive analysis.

- CONTRACTOR REPORT.
  Scientific and technical findings by NASA-sponsored contractors and grantees.

- CONTRACTOR REPORT.
  Scientific and technical findings by NASA-sponsored contractors and grantees.

- CONFERENCE PUBLICATION.
  Collected papers from scientific and technical conferences, symposia, seminars, or other meetings sponsored or co-sponsored by NASA.

- SPECIAL PUBLICATION.
  Scientific, technical, or historical information from NASA programs, projects, and missions, often concerned with subjects having substantial public interest.

- TECHNICAL TRANSLATION.
  English-language translations of foreign scientific and technical material pertinent to NASA's mission.

Specialized services also include organizing and publishing research results, distributing specialized research announcements and feeds, providing information desk and personal search support, and enabling data exchange services.

For more information about the NASA STI program, see the following:

- Access the NASA STI program home page at http://www.sti.nasa.gov

NASA/TM-20240003659

# Design of an In-Slot Cooled Air-Core Flux-Focusing Permanent Magnet Synchronous Machine for Electric Aircraft Applications

*Jonathan Gutknecht, Thomas Tallerico, and Aaron Anderson*
*Glenn Research Center, Cleveland, Ohio*

National Aeronautics and
Space Administration

Glenn Research Center
Cleveland, Ohio 44135

May 2024

This work was sponsored by the Advanced Air Vehicles Program
at the NASA Glenn Research Center.

*Level of Review*: This material has been technically reviewed by technical management.

This report is available in electronic form at https://www.sti.nasa.gov/ and https://ntrs.nasa.gov/

NASA STI Program/Mail Stop 050
NASA Langley Research Center
Hampton, VA 23681-2199

# Design of an In-Slot Cooled Air-Core Flux-Focusing Permanent Magnet Synchronous Machine for Electric Aircraft Applications

Jonathan Gutknecht, Thomas Tallerico, and Aaron Anderson
National Aeronautics and Space Administration
Glenn Research Center
Cleveland, Ohio 44135

## Abstract

High performance and reliable permanent magnet synchronous machines are potentially a key technology for enabling reduced emissions in future generations of sustainable aircraft. In this paper, a novel air-core flux focusing permanent magnet synchronous machine with carbon fiber shafting for aviation applications is presented. A low-fidelity analytical sizing tool is detailed for the motor topology. The sizing tool is used to explore design trades and create an example 100 kW flux-focusing motor for eVTOL applications. Higher fidelity finite element analysis was used to validate the predicted performance of the motor. The selected design is able to achieve roughly 97 percent efficiency and 6 kW/kg at a continuous operating power of 100 kW.

## 1.0 Introduction

The aviation industry has set reduced emission targets for the next generation of aircraft. Electrification and/or hybridization of aircraft powertrains is a possible path to achieving these emission goals. High performance electric motor drivetrains are needed to enable electrified aircraft to meet emission goals without sacrificing aircraft performance.

Permanent magnet synchronous machines (PMSM) are commonly seen as the non-cryogenic motor technology most capable of meeting the performance needs of electrified aircraft (Refs. 1 and 2). Numerous designs and design studies have been completed on permanent magnet synchronous machines for aircraft applications (Refs. 3 to 9). Often these designs converge to Halbach arrays rotor magnet arrangements (Refs. 4 to 6, and 9). The authors in Reference 10 found that for a particular machine design application, an air-core flux-focusing rotor topology (Figure 1) was able to outperform a Halbach array and other permanent magnet rotor topologies. The target machine design for that study, however, was for a relatively low power and was constrained to a small diameter.

In this paper, a more complete study of the air-core flux-focusing PMSM is completed. An analytical design tool for the machine topology is detailed and applied to an example application of a 100 kW motor relevant to electric vertical take-off and landing (eVTOL) or Urban Air Mobility (UAM) applications. The motor is assumed to be geared and an estimation of gearbox performance is included in the design tool to constrain the optimization of the drivetrain. Design trade space studies are completed with the analytical design tool. Finite element analysis (FEA) is used to validate the analytical design tool results and refine the machine design.

Section 2.0 of this paper presents the formulation of the analytical design tool. Section 3.0 presents the design studies completed with the tool. Section 4.0 covers the 2D FEA model and refinement of the design. Section 5.0 presents the selected design and detailed analysis of the carbon fiber shaft.

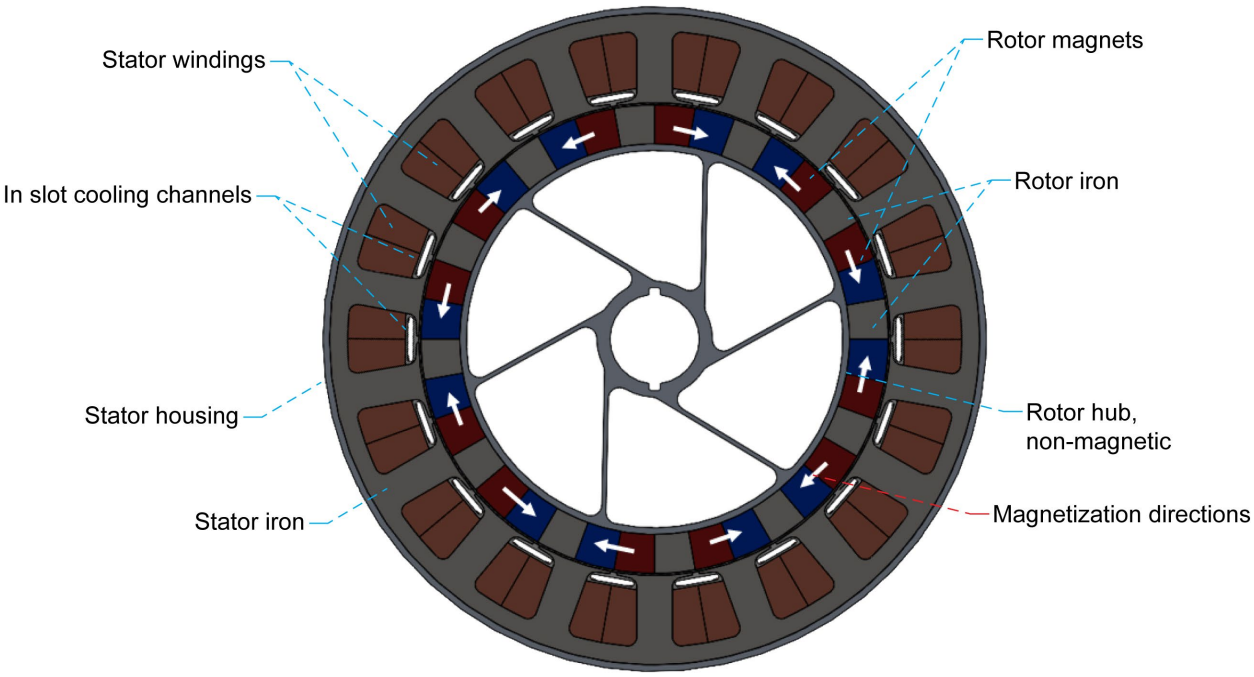


Figure 1.—Cartoon of Air-core Flux-Focusing PMSM.

## 2.0 Analytical Design Tool

The developed design tool for air-core flux-focusing PMSMs is depicted graphically in Figure 2. The tool uses a genetic algorithm to quantify the achievable performance of the motor drivetrain topology in terms of mass and efficiency. The genes used to define the machine designs in the optimization are listed in Table I. Magnetic, thermal, and mechanical analyses are completed in the fitness evaluation of the genetic algorithm to obtain a prediction of machine performance and mass. Gearbox mass and efficiency estimates are made for a given motor design using gearbox optimization results produced using the methodology described in Reference 11. The motor inverter is neglected in this initial version of the design tool. The design tool in this initial form designs the motor for a single continuous operating point. Adding the inverter into the design tool and extending it to mission profile optimization as was done in References 7 and 12 will be the target of future work. The bulk of the methods used in the design tool to estimate motor performance are detailed by the authors in Reference 13. Summaries of the methods are provided in the subsequent sections. Readers are pointed to that reference for more complete discussions of the methods.

### 2.1 Gearbox Mass and Efficiency Estimation

Gearboxes are pre-optimized using the method described in Reference 11. Three types of gearboxes were considered: single stage planetary, two stage planetary, and a first stage planetary second stage spur gear configuration. The gearboxes were sized for 5000 hr of life at 100 kW and 1000 rpm output speed. Gearbox mass and efficiency for a given fitness evaluation are estimated using a scattered interpolant function with inputs of motor rpm and specific torque index. The data points defining the scattered interpolant are depicted in Figure 3. Motor rpm dictates the gear ratio of the gearbox, and specific torque index dictates the trade between gearbox mass and efficiency for a given gear ratio.

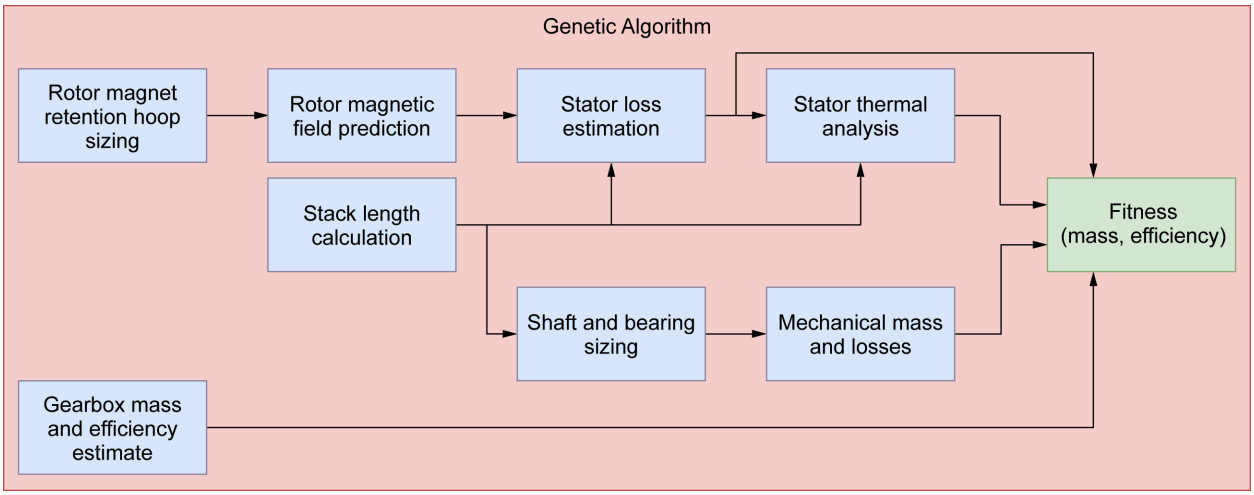


Figure 2.—Design Tool Flow Diagram.

TABLE I.—GENETIC ALGORITHM VARIABLES

| Variable | Physical meaning |
|---|---|
| $B_{\text{back iron}}$ | Flux density of stator back iron (T) |
| $B_{\text{stator tooth}}$ | Flux density of stator tooth (T) |
| $B_{\text{rotor iron}}$ | Flux density of rotor iron (T) |
| $v_{\text{tip}}$ | Magnet tip speed (m/s) |
| $n$ | Rotational speed (rpm) |
| $f_{\text{elec}}$ | Frequency of magnetization due to windings (Hz) |
| $m_{EM}$ | Mass of electromagnetic components (kg) |
| $t_{\text{stator}}$ | Stator thickness (m) |
| $t_{\text{magnet}}$ | Magnet thickness (m) |
| $t_{\text{cooling}}$ | Cooling channel thickness (m) |
| $k$ | Specific torque index |
| $Q_{\text{fluid}}$ | Fluid flow rate (L/min) |

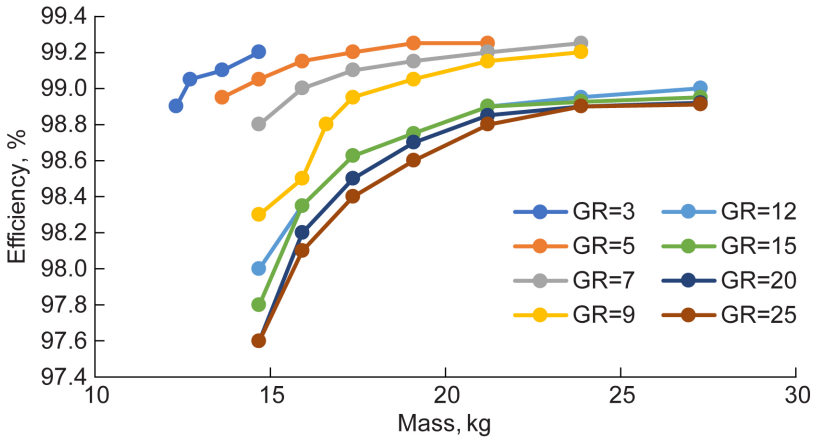


Figure 3.—Gearbox Mass and Efficiency Scattered Interpolant Data Points.

## 2.2 Rotor Retention

Because no rotor back iron is used in the air-core flux focusing rotor topology, a carbon fiber retaining hoop around the rotor is used to retain the magnets and rotor iron pole pieces. To determine the required hoop thickness, the centripetal loading created by the rotor magnetic components is calculated. The outer radius of the magnetic components $R_m$ needed to achieve the desired tip speed at the specified rpm is calculated based on the genetic algorithm inputs as

$$R_m = \frac{v_{\text{tip}}}{\omega} = \frac{v_{\text{tip}}}{n\frac{2\pi}{60}} \tag{1}$$

where ω is the rotor angular velocity. The mass of the rotor magnetic components per meter can then be estimated as

$$\lambda_{\text{rotor}} = \rho_{\text{iron}} * \pi\left(R_m^2 - R_r^2\right) = \rho_{\text{iron}} * \pi\left(R_m^2 - \left(R_m - t_{\text{magnet}}\right)^2\right) \tag{2}$$

Where $\lambda_{\text{rotor}}$ is the rotor magnetic component mass per meter, $\rho_{\text{iron}}$ is the density of the rotor iron and $R_r$ is the inner radius of the magnets. In Equation (2), the rotor is approximated to be all iron as the relative ratio of magnet to rotor iron is not known until Equation (12) below is solved. The force per unit length that the rotor will exert on the inside of the retaining hoop is equal to the centripetal force per unit length that the hoop exerts on the rotor and can be approximated as

$$F_\lambda = \lambda_{\text{rotor}} \frac{R_m + R_r}{2} \omega^2 \tag{3}$$

The pressure exerted on the internal face of the hoop can then be calculated as

$$P_{\text{hoop}} = \frac{F_\lambda}{2\pi R_m} \tag{4}$$

The required hoop thickness to withstand the pressure is estimated as

$$t_{\text{hoop}} = \frac{2R_m P_{\text{hoop}}}{2\sigma_{\text{max}}} \tag{5}$$

where $\sigma_{\text{max}}$ is the max allowable stress in the hoop. In this paper, the retaining hoop is assumed to be made from carbon fiber with a minimum thickness of 0.25 mm, layer thicknesses of 0.125 mm, and max allowable stress of 800 MPa. Additional material assumptions are summarized in Table III. Since the carbon fiber hoop sits in the airgap of the machine and has a permeability matching that of air, the thickness of the retaining hoop is added to the assumed mechanical airgap between the rotor and stator in the tool for all magnetic calculations.

## 2.3 Rotor Magnetic Field Calculations

The field produced by the rotor is calculated using a basic magnetic circuit model of a single pole of the machine. The magnetic reluctance network used is depicted graphically in Figure 4. Lipo (Ref. 14) gives a complete solution for a rotor topology of this type when all the magnets touch at the inner magnetic diameter of the rotor (i.e., rotor iron width is zero at the inner magnetic diameter). This maximizes the amount of magnetic material for a given rotor volume and is an optimum solution for high power density machines. In this paper the goal, however, is specific power, so the approach presented by Lipo is generalized to allow rotor magnet inner diameter to be independent of the width of the magnets and pole count of the machine.

Rotor pole count is back calculated from the rotational speed and electrical frequency genetic optimization variables as

$$p = 2 * \text{round}\left(\frac{60}{n} * f_{\text{elec}}\right) \tag{6}$$

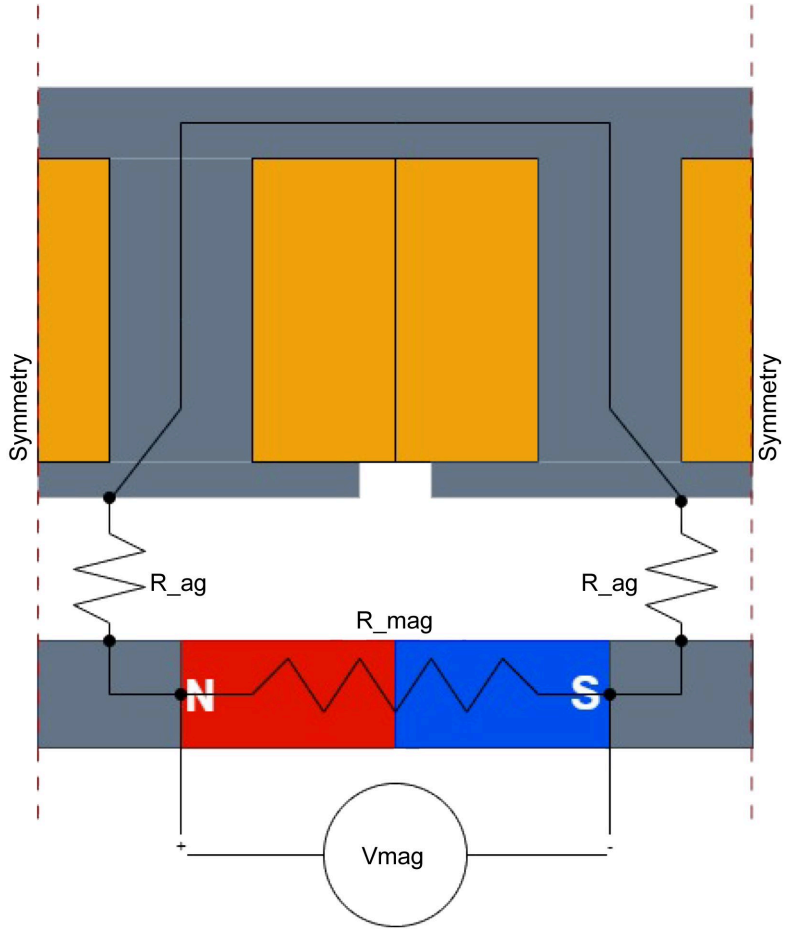


Figure 4.—Magnet Reluctance Circuit Graphical Depiction.

to ensure that the design uses an even number of poles. The electrical frequency of the machine is then calculated using the calculated number of poles as

$$f_{\text{elec}} = \frac{n}{60}\frac{p}{2} \tag{7}$$

The width of each magnetic pole along the outer diameter of the rotor, $w_{\text{pole}}$, is given by

$$w_{\text{pole}} = \frac{2\pi R_m}{p} \tag{8}$$

Solving the magnetic reluctance network in Figure 4 assuming the iron is infinitely permeable, and the magnet has a relative permeability of 1 gives the field in the magnet as

$$B_{\text{magnet}} = \frac{B_r w_{\text{magnet}}}{w_{\text{magnet}} + 2t_{\text{ag}}} \tag{9}$$

and the field in the rotor iron at the airgap as

$$B_{\text{rotor iron}} = \frac{B_r w_{\text{magnet}}}{\frac{w_{\text{iron}}}{2}\frac{w_{\text{magnet}}}{t_{\text{magnet}}} + 2t_{\text{ag}}} \tag{10}$$

where $B_r$ is the remanence of the rotor magnets, $t_{\text{ag}}$ is the total airgap thickness, $B_{\text{magnet}}$ is the field in the magnet, $B_{\text{rotor iron}}$ is the field in the rotor iron at the airgap, $w_{\text{magnet}}$ is the width of the magnet, and $w_{\text{iron}}$ is the circumferential width of the rotor iron at the outer radius of the machine. $w_{\text{magnet}}$ and $w_{\text{iron}}$ are related by

$$w_{\text{pole}} = w_{\text{iron}} + w_{\text{magnet}} \tag{11}$$

For a target value of $B_{\text{rotor iron}}$, $w_{\text{iron}}$ can be found by plugging Equation (11) into (10)and rearranging Equation (10) so that it takes a quadratic form

$$ax^2 + bx + c = 0 \tag{12}$$

with

$$x = \text{iron percent inner} = \frac{w_{\text{iron}}}{w_{\text{pole}}} \tag{13}$$

$$a = \frac{w_{\text{pole}} B_{\text{rotor iron}}}{t_{\text{magnet}}} \tag{14}$$

$$b = -\left[\frac{B_{\text{rotor iron}}}{t_{\text{magnet}}} + 2B_r\right] \tag{15}$$

$$c = -4\frac{t_{\text{ag}} B_{\text{rotor iron}}}{w_{\text{pole}}} + 2B_r \tag{16}$$

Solving for x defines the magnet width and the iron width. Designs that result in no real solutions to Equation (12) are assumed to not close and are assigned baseline mass and efficiency values in the genetic algorithm.

The peak magnitude of the fundamental harmonic of the flux density in the airgap is estimated as given in Reference 14 as

$$B_{g1} = B_{\text{rotor iron}} * \frac{4}{\pi} \sin\left( \text{iron percent inner} * \frac{\pi}{2} \right) \tag{17}$$

The average flux density in the airgap is calculated as

$$\overline{B} = B_{\text{rotor iron}} * (\text{iron percent inner}) \tag{18}$$

In order to achieve the desired flux densities in the stator iron defined by the genetic algorithm variables, the stator back iron thickness is calculated per the method described in Reference 13 as

$$t_{\text{stator back iron}} = \frac{\pi R_S \overline{B}}{p B_{\text{back iron}}} \tag{19}$$

The stator tooth thickness in the case of distributed windings when slots per pole is equal to 3 is given by

$$t_{\text{stator tooth}} = \frac{\pi R_S \overline{B}}{p B_{\text{stator tooth}}} \tag{20}$$

In the case of concentrated windings when the slots per pole is less than 2, the stator tooth thickness is given by

$$t_{\text{stator tooth}} = \frac{2\pi R_S \overline{B}}{p B_{\text{stator tooth}}} \tag{21}$$

## 2.4 Stack Length and Mass Calculation

Since motor magnetic mass as a genetic optimization variable, motor stack length is back calculated to achieve the target magnetic mass in each fitness evaluation based on the mass of the end windings and the mass per meter of the magnetic components.

The inner radius of the stator is calculated as

$$R_{\text{is}} = R_m + t_{\text{ag}} \tag{22}$$

and the outer radius is given by

$$R_{\text{os}} = R_{\text{is}} + t_{\text{stator}} \tag{23}$$

The cross-sectional areas of the stator back iron, stator tooth tips, and stator teeth are given by

$$A_{\text{back}} = \pi\left(R_{\text{os}}^2 - \left(R_{\text{os}} - t_{\text{stator back iron}}\right)^2\right) \tag{24}$$

$$A_{\text{tip}} = \pi\left(\left(R_{\text{is}} + t_{\text{tip}}\right)^2 - R_{\text{is}}^2\right) \tag{25}$$

and

$$A_{\text{tooth}} = \text{Slots} * t_{\text{stator tooth}} * \left(t_{\text{stator}} - t_{\text{stator back iron}} - t_{\text{tip}}\right) \tag{26}$$

respectively. The stator winding area is then calculated as

$$A_{\text{winding}} = A_{\text{stator}} - A_{\text{iron}} = \pi\left(R_{\text{so}}^2 - R_{\text{is}}^2\right) - \left(A_{\text{back}} + A_{\text{tip}} + A_{\text{tooth}}\right) \tag{27}$$

For distributed windings with full pole pitch, the length of the end windings between two slots for the same phase are approximated as forming the two sides of an equilateral triangle. The total length of an end winding is then

$$l_{\text{end winding}} = \frac{2\pi R_{\text{os}}}{p * \cos\left(\frac{\pi}{3}\right)} \tag{28}$$

For concentrated windings the end winding length is estimated as

$$l_{\text{end winding}} = \frac{\frac{2\pi R_{\text{os}}}{\text{slots}} + t_{\text{stator tooth}}}{2} * \frac{\pi}{2} \tag{29}$$

The mass of the end windings is estimated as

$$m_{\text{end winding}} = l_{\text{end winding}} A_{\text{winding}} \rho_{\text{winding}} \tag{30}$$

with $A_{\text{winding}}$ being the cross-sectional area of windings in the stator and $\rho_{\text{winding}}$ being the density of windings assuming a 50 percent copper fill. The stack length of the machine is calculated to meet the specified electromagnetic mass using the formula

$$L = \frac{m_{\text{EM}} - m_{\text{end winding}}}{\rho_{\text{iron}} A_{\text{rotor iron}} + \rho_{\text{iron}} A_{\text{stator iron}} + \rho_{\text{winding}} A_{\text{winding}} + \rho_{\text{magnet}} A_{\text{magnet}}} \tag{31}$$

where $A_{\text{rotor iron}}$ is the total cross-sectional area of iron in the rotor, $A_{\text{stator iron}}$ is the total cross-sectional area of iron in the stator, and $A_{\text{magnet}}$ is the total cross-sectional area of magnets in the rotor.

## 2.5 Stator Losses

In this design tool, stator losses are the only magnetic electromagnetic loss accounted for as rotor magnetic losses are assumed to be small due to the small amount of time varying flux in the rotor and the use of fine laminations in the rotor magnetic components. Stator iron magnetic losses are estimated using the Steinmetz equation:

$$P_v = kf^{\alpha}B^{\beta} \tag{32}$$

Where $P_v$ is the energy loss per unit mass, $f$ is the frequency of the magnetic field, $B$ is the peak magnetic flux density, and $k$, $\alpha$, and $\beta$ are Steinmetz coefficients found by curve fitting to experimental loss measurements (Ref. 15). The frequency of the magnetization of the stator iron is estimated by the rate that a given stator tooth engages a rotor pole so that

$$f_{\text{iron}} = f_{\text{elec}} * \frac{\text{Slots}}{\frac{p}{2}} \tag{33}$$

or

$$f_{\text{iron}} = f_{\text{elec}} * \frac{W_{\text{pole}}}{w_{\text{iron}}} \tag{34}$$

whichever of the two is greater. Since the iron magnetization repetition frequency is at the pole passage frequency the overall iron loss equation is given by

$$\text{LOSS}_{\text{iron}} = \frac{f_{\text{elec}}}{f_{\text{iron}}} V_{\text{iron}} k f_{\text{iron}}^{\alpha} B_{\text{iron}}^{\beta} \tag{35}$$

where $V_{\text{iron}}$ is the volume of the iron (Ref. 14). Iron losses are calculated for the tooth and the back iron separately since different flux densities are allowed in the tooth and back iron by the design tool.

The required stator current is calculated by back solving the $D^2L$ motor sizing equation for the electrical loading $\bar{A}$ in the machine (Ref. 16). The formulation of the $D^2L$ sizing equation used here is

$$P = \tau\omega = \omega\frac{\pi^2}{8} B_{g1} \bar{A} D^2 L \tag{36}$$

where $P$ is the motor power, $\tau$ is the motor torque, $\omega$ is the rotor angular velocity, $\bar{A}$ is the stator electrical loading, $D$ is the inner diameter of the stator, and $L$ is the stack length of the motor. The above combines the two different forms of $D^2L$ from References 14 and 16 so that $B_{g1}$ and $\bar{A}$ can be used in the formulation (Ref. 13). $\bar{A}$ can be used to calculate DC resistive losses in the stator using the method described in Reference 13. First $\bar{A}$ is used to calculate the average total current in the stator using

$$\bar{A} = \frac{k_w I_{\text{tot}}}{\pi D} \tag{37}$$

where $I_{\text{tot}}$ is the total current that passes through the stator and $k_w$ is the winding factor. The winding factor depends on the slots per pole of the motor per phase of the electric signal. Typical values of $k_w$ for concentrated windings range from 0.85 to 0.95, and typical values for distributed full pitch windings

range from 0.95 to 1.00. In this paper $k_w$ is taken to be 1 for distributed windings and 0.866 for concentrated windings a 0.5 slot per pole per phase winding combination is assumed. The average current in each winding layer per slot can be calculated from $I_{tot}$ as

$$I_{\text{avg, layer}} = \frac{I_{\text{tot}}}{\text{slots} * \text{layers}} \tag{38}$$

where $I_{\text{avg,layer}}$ is the average current in a given winding layer over time, slots is the number of slots in the machine, and layers is the number of winding layers in each slot. For sinusoidal current the average current in a layer can be converter to root mean square current using

$$I_{\text{rms, layer}} = \frac{\pi}{2} \frac{I_{\text{avg, layer}}}{\sqrt{2}} \tag{39}$$

where $I_{\text{rms,layer}}$ is the root mean squared current in each winding layer.
The resistive losses in the windings can then be found using

$$P_{\text{loss},I^2R} = \text{slots} * \text{layers} * \rho_{\text{copper}} \frac{\left(L + l_{\text{end winding}}\right)}{\text{fill} * A_{\text{layer}}} * I^2_{\text{rms, layer}} \tag{40}$$

where $\rho_{\text{copper}}$ is the resistivity of copper.

## 2.6 Thermal Resistance Model

A 2D thermal reluctance network model is used to predict the iron and winding temperatures under steady state operation for a given design output by the genetic algorithm. Designs which are calculated to have steady state operating temperatures in the windings greater than the maximum allowable temperature given in Table III are assigned baseline fitness values in the genetic algorithm. Due to the symmetry of the stator, only one half of one slot of the machine is used for the thermal model. Figure 5 shows the geometry and layout of thermal resistances used. An in-slot cooling topology with cooling at only the bottom of the winding slot is assumed for this initial motor design. In-slot cooling improves the thermal performance of the machine and correspondingly improves achievable specific power at the cost of added iron losses at a given mass due to larger slots and thicker overall stators (Ref. 17). The bottom of the slot variant of in-slot cooling is assumed because per (Ref. 10) it was found that with the cooling channel occupying the bottom of the slot AC losses in hairpin windings were sufficiently low to outperform stranded or litz wire. Hairpin windings are not assumed in this design, however, as a more complicated magnetic reluctance network model would be needed to solve for the AC losses that arise due to the increase in copper fill percentage. A future iteration of the design tool will incorporate AC winding losses. The thermal reluctance values are populated using the equations for thermal resistances and cooling flows found in Reference 13. Appendix A provides a summary of the thermal reluctance model equations.

## 2.7 Shaft and Bearing Sizing

Bearings and shafts are co-designed in the design tool and are included in the mass estimate of the machine. Bearing losses are also calculated and incorporated in the efficiency estimate. Design is completed per the methods described in Reference 13. Table II provides the assumed loading profile for the bearings.

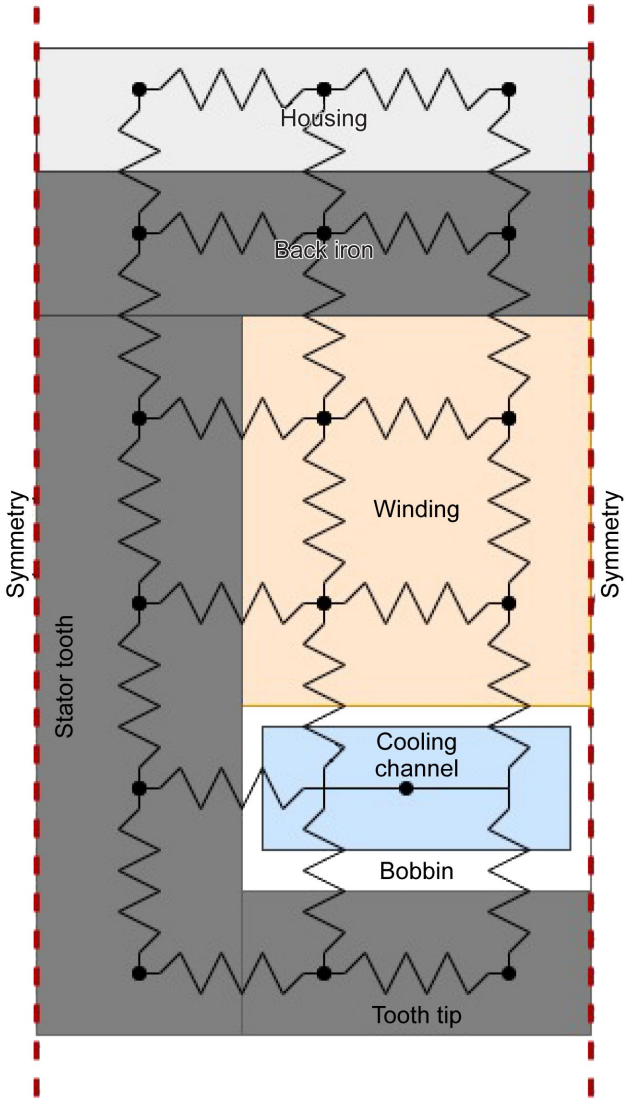


Figure 5.—2D Thermal Reluctance Network of Half Stator Slot.

TABLE II.—PEAK AND NOMINAL VALUES OF ASSUMED LOADING PROFILE ON BEARINGS

| | Peak values | Nominal values |
|---|---|---|
| Yaw rate | 2.5 rad/s | 0 |
| Pitch rate | 1 rad/s | 0 |
| Roll rate | 0 | 0 |
| Acceleration | 2.5g | 1g |
| Percent of life | 10% | 90% |

Bearings loads are calculated based on the estimated mass, moments of inertia, and rotational speed of the rotor. Lifetime calculations are then carried out for a dataset of bearings from Reference 18. A minimum required life of 10,000 hr and 99 percent reliability was used. A shaft is sized for all bearings that meet the life requirements. For metal shafts, the bearing bore diameter is used as the outer diameter of the shaft. For carbon fiber shafts, the shaft is assumed to be 2 mm smaller in diameter than the bearing bore diameter to allow for the use of steel sleeves on top of the carbon fiber to interface with the bearings. In this initial design tool, for the purpose of predicting shaft critical speed, the carbon fiber shaft is assumed to be a straight shaft, neglecting the increase in diameter to match the inner diameter of the rotor. When predicting the mass of the shaft, however, the true geometry of the carbon fiber shaft is accounted for.

Since the motor in this paper is assumed to be a geared high-speed machine, the shaft is assumed to be sized primarily by critical speed. The critical speed of the shaft is estimated as

$$\frac{1}{N_{c,\text{rotor}}^2} = \frac{1}{N_{c,\text{disk}}^2} + \frac{1}{N_{c,\text{straight shaft}}^2} \tag{41}$$

where $N_{c,\text{disk}}$ is the critical speed for a rotor whose mass is centered in a disk positioned at the middle of the shaft and $N_{c,\text{straight shaft}}$ is the critical speed of the shaft on its own (Ref. 19). $N_{c,\text{disk}}$ is given by

$$N_{c,\text{disk}} = \frac{60}{2\pi} * \sqrt{\frac{192EI}{m_{\text{disk}} L^3}} \tag{42}$$

where $E$ is the elastic modulus of the shaft material, $I$ is the second area moment of inertia of the straight shaft, $m_{\text{disk}}$ is the mass of the disk rotor, and $L$ is the length of the shaft between the two supports (Ref. 20). $N_{c,\text{straight}}$ shaft is given by

$$N_{c,\text{straight shaft}} = 60 * 1.57 \frac{\sqrt{\frac{EI}{m_{shaft}}}}{L^2} \tag{43}$$

As a conservative approach, the first critical speed of the rotor in the code is required to be two times higher than the rotational speed of the motor. The above critical speed estimate does not account for the stiffness of the bearings or the surrounding structure and correspondingly will overestimate the first critical speed when the motor is installed on an aircraft. Sizing for two times the motor speed ensures that the critical speed will stay above operating even when the surrounding stiffness is accounted for or if there is an overspeed event.

If no set of bearings and corresponding shaft design are able to close the overall motor design is assigned a minimum fitness in the genetic algorithm. If multiple bearing and shaft designs close, a design is selected based on minimizing the weight of the shaft, bearings, and end bells of the machines. Bearing losses are then estimated using the equations found in Reference 21 and included in the efficiency estimate for the machine.

## 2.8 Fitness Definition

The genetic algorithm used maximizes each fitness value, so the fitness of a design is the combined efficiency of the motor and gearbox and the negative sum of the motor and gearbox mass. Designs that failed to close were assigned baseline mass and efficiency values. The final output of the design tool is a pareto front consisting of the mass and efficiency values of the best designs the genetic algorithm was able to find.

## 3.0 Motor Sizing Results

The assumptions and requirements used for the motor design completed in this paper are summarized in Table III. The target power and rotor rotational speed are taken to be in line with NASA's revolutionary vertical lift concept vehicles (Refs. 22 and 23) and past vertical lift drivetrain design studies (Refs. 12 and 24). Since the motor inverter is not accounted for in this initial design tool and studies, a limit on electrical frequency of 1000 Hz is applied. This frequency is lower than is feasible for SiC based inverter drives; however, this limit was imposed because in References 12 and 24 it was found that motor drivetrain mission efficiency for eVTOL applications decayed significantly with increased motor electrical frequency.

A SmCo magnet material with an effective magnet remanent flux density ($B_r$) of 1 T is assumed. A remanent flux density value of 1 T is a conservative estimate and accounts for both a reduction in the magnet performance due to temperature and loss of magnet fill due to the use of magnet laminations. 2 mm magnet laminations are assumed when predicting magnet loss in Section 4.0.

Four design studies were completed to refine the topology of the machine design and select a motor design for further refinement. The four studies were:

1. Distributed versus concentrated windings
2. Shaft material
3. Laminar versus turbulent flow
4. Flux Focusing versus Halbach topology

Each optimization was run with a population of 600 designs for 300 generations. Table IV provides the optimization variable ranges used. The following sections present the results of each study in sequence.

TABLE III.—ASSUMPTIONS AND REQUIREMENTS FOR EXAMPLE MOTOR

| | | | |
|---|---|---|---|
| Power | 100 kW | Magnet material | SmCo |
| Gearbox output RPM | 1000 rpm | Magnet effective *Br* | 1 T |
| Max electrical frequency | 1000 Hz | Magnet density | 8300 kg/m$^3$ |
| Cooling approach | Bottom of slot | Retaining hoop material | IM7 Carbon Fiber |
| Bobbin material | AlN | Max hoop stress | 800 MPa |
| Bobbin wall thickness | 1 mm | Hoop layer thickness | 0.125 mm |
| Min channel size | 1 mm | Iron loss coefficients: | ---------- |
| Cooling fluid | 60 to 40 PGW | *k* | 0.0015 |
| Tooth tip thickness | 1.5 mm | α | 1.5 |
| Copper winding fill | 50% | β | 1.6 |
| Copper temperature for loss calculator | 150 °C | Iron thermal conductivity | 25 W/mK |
| Epoxy density | 2730 kg/m$^3$ | Max flux density | 2 T |
| Epoxy thermal conductivity | 1.9 W/mK | Housing material | Aluminum |
| Max winding temperature | 170 °C | Housing clearance to windings | 25 mm |

TABLE IV.—RANGE OF EACH OPTIMIZATION VARIABLE ALLOWED IN DESIGN TOOL

| Optimization variable | Range |
|---|---|
| $B_{\text{back iron}}$ | 1.5 to 2 T |
| $B_{\text{stator tooth}}$ | 1.5 to 2 T |
| $B_{\text{rotor iron}}$ | 1 to 2 T |
| $v_{\text{tip}}$ | 50 to 200 m/s |
| $n$ | 3,000 to 20,000 rpm |
| $f_{\text{elec}}$ | 700 to 1,000 Hz |
| $m_{EM}$ | 5 to 35 kg |
| $t_{\text{stator}}$ | 8 to 35 mm |
| $t_{\text{magnet}}$ | 5 to 25 mm |
| $t_{\text{cooling}}$ | 1 to 5 mm |
| $k$ | 0 to 1 |
| $Q_{\text{fluid}}$ | 1 to 300 L/min |

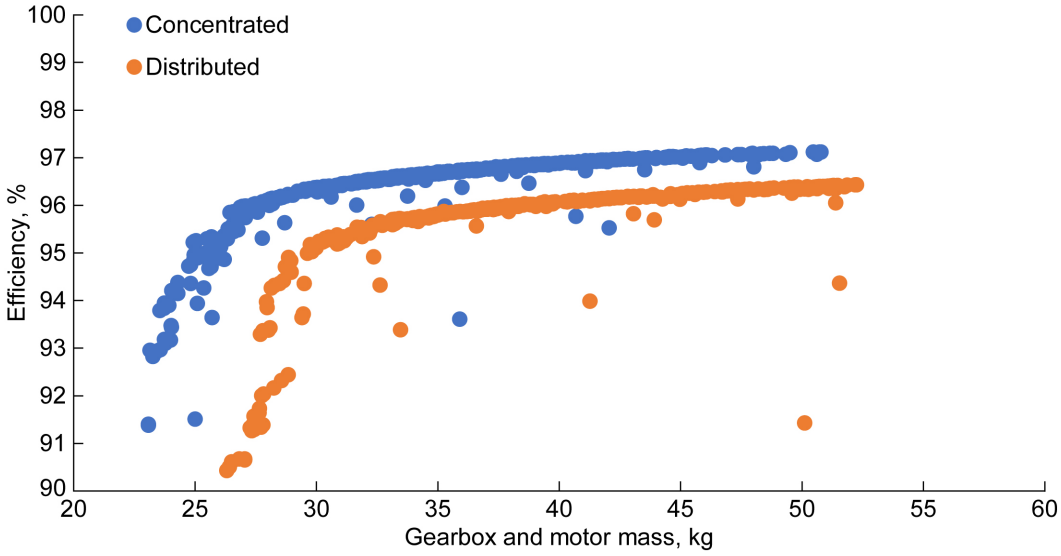


Figure 6.—Comparison of Efficiency and Mass for Concentrated and Distributed Winding Motors.

## 3.1 Distributed Versus Concentrated Windings

In Reference 10, it was found that distributed windings had significant benefit over concentrated windings for a specific application where diameter was constrained to small values and the length to diameter ratio was large. In the current work, the diameter is a free variable, so the trade was revisited. The design tool was run for both concentrated and distributed windings assuming a carbon fiber shaft and laminar cooling flow. For distributed windings, a 1 slot per pole per phase winding layout and a winding factor of 1 was assumed. For concentrated windings, a 1/2 slot per pole per phase winding layout and a winding factor of 0.866 was assumed. Figure 6 shows the results of running the optimization. Concentrated windings are shown to outperform distributed windings by about 1 percent efficiency for a given mass. The higher performance of concentrated windings in this case results from the smaller end winding lengths relative to the active length of the machines outweighed the winding factor

improvements provided by the distributed windings for the size and aspect ratio of machine that was optimum in the design tool.

## 3.2 Carbon Fiber Versus Titanium Shafting

Due to the elimination of the rotor back iron, eddy currents in the rotor body and shaft become a concern for the air-core flux-focusing rotor topology. Additionally, steels with relative magnetic permeability greater than 1 will create a leakage path through the shaft for the rotor magnet flux and reduce machine performance. Design tool studies were completed assuming carbon fiber, 316 stainless steel, and titanium shafts. Concentrated windings and laminar cooling flow were assumed. Figure 7 shows the results of the optimization for each shaft type. A minor reduction in mass for a given efficiency is observed in the results for carbon fiber relative to titanium and stainless. Figure 8 shows that the carbon

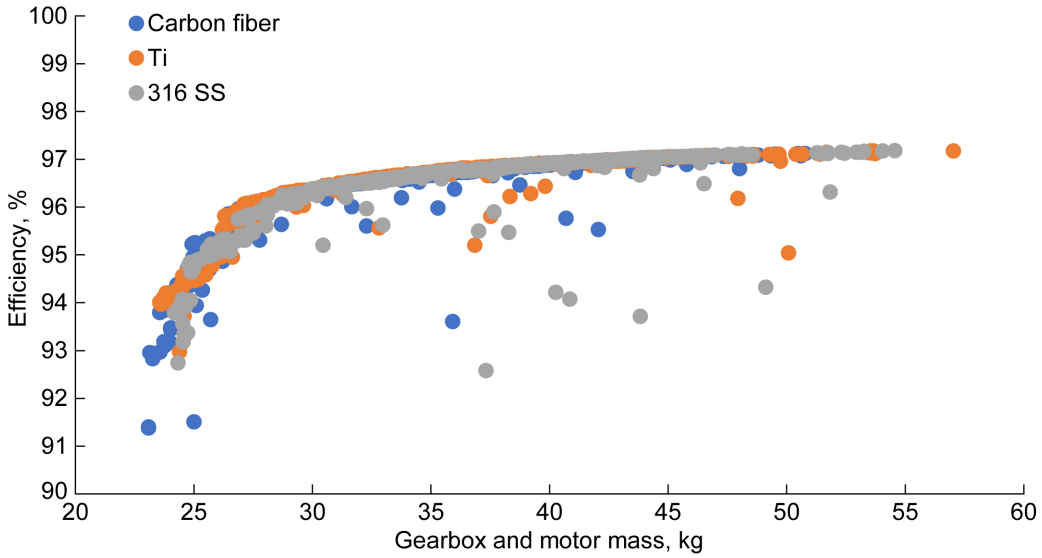


Figure 7.—Comparison of Efficiency and Mass for Motors with Titanium, 316 Stainless Steel, and Carbon Fiber Shafts.

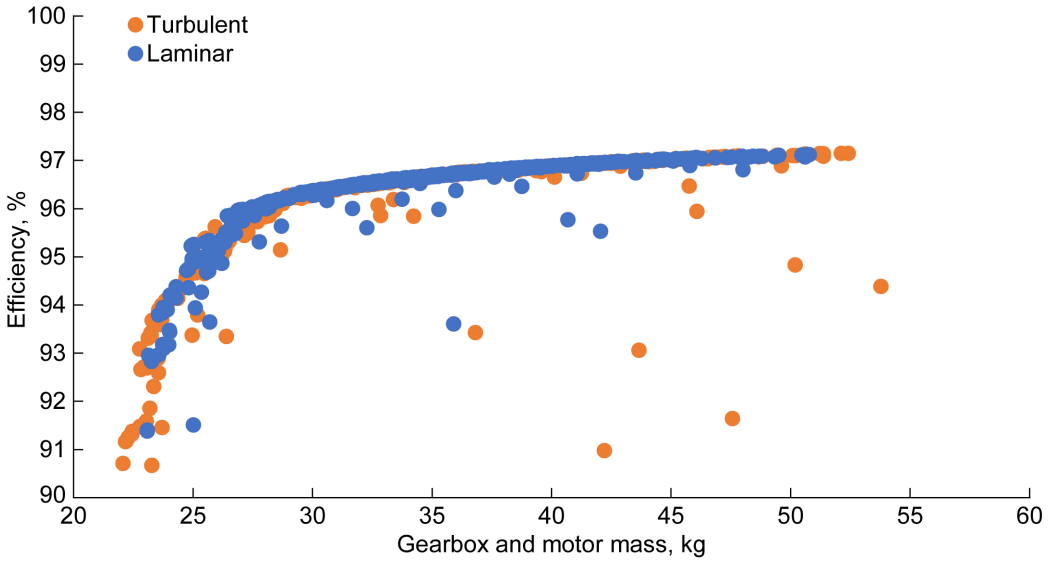


Figure 8.—Motor and Gearbox Mass vs Motor Rotation Speed for Motors with Titanium, 316 Stainless Steel, and Carbon Fiber Shafts.

fiber shafts optimized to slightly lower speeds than their metal counter parts. This lower speed results from the lower stiffness of carbon fiber relative to the metals and the corresponding higher difficulty carbon fiber has in suppressing shaft critical speeds. However, as noted in Section 2.7, the design tool's shaft model assumes a straight shaft and doesn't fully capture the complex geometry of the carbon fiber shaft. Section 4.3 shows that with accurate geometry for the design, shaft bending modes are higher than predicted for the tool and correspondingly there may be opportunity to refine the design tool model and achieve higher speeds with the carbon fiber shaft. In Section 4.2, transient FEA is carried out on the selected design to assess the eddy current losses in the shaft for different metals to further explore whether carbon fiber shafting has performance benefit for the air core flux focusing machine topology.

## 3.3 Laminar Versus Turbulent Flow

Designing a motor with laminar flow typically eases integration into an overall aircraft as flow losses in the cooling path and correspondingly required pumping power for the fluid flow loop is easily predicted. Turbulent flow, however, is able to improve the thermal performance of a machine and allows a machine to close at a lower mass with higher losses. Design studies were carried out with the design tool to compare laminar and turbulent flow performance for the machine. Design studies were carried out for different minimum fluid flow channel thicknesses of 1, 2, and 3 mm. Figure 9 shows a comparison of turbulent and laminar flow with a 1 mm minimum channel size, Figure 10 shows a comparison of laminar and turbulent flow with all minimum channel sizes studied, and Figure 11 shows a comparison of turbulent flow results for different channel sizes.

In Figure 9 with 1 mm channels, no difference between the two flow types is shown for high mass and high efficiency designs. Turbulent flow, however, is able to close designs at lower masses and corresponding lower efficiencies than the laminar flow designs. In Figure 10, a significant drop off of about 2 kg per mm increase in channel size is shown for the lowest weight design that laminar flow is able to close. This corresponds to the Nusselt number being limited by the designs not being able to achieve as high of ratios of *b/a* in Equation (50) due to the larger minimum channel size and slot width being constrained by the motor electromagnetic design. Turbulent flow results in Figure 11 shows less

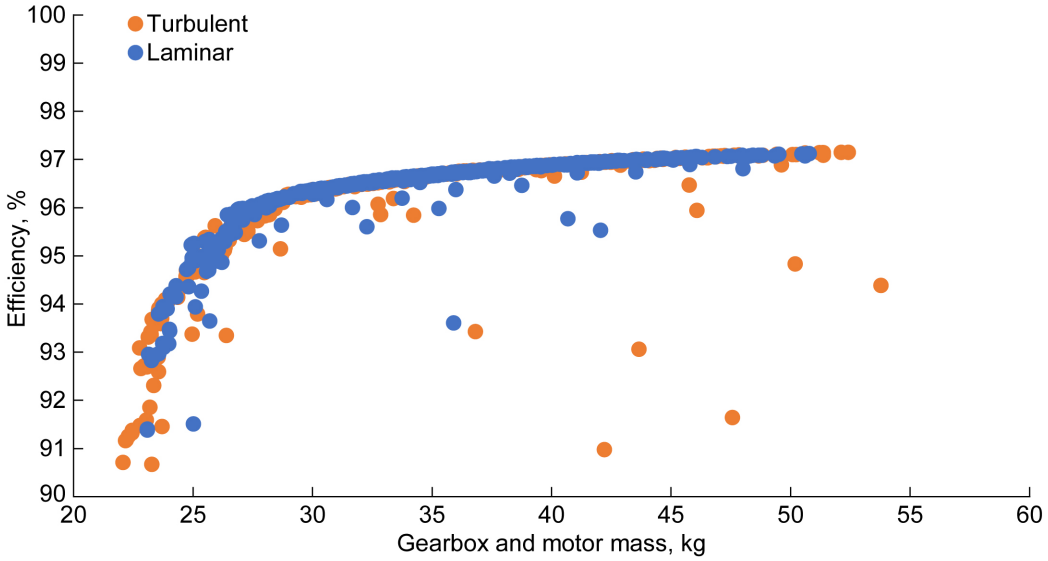


Figure 9.—Comparison of Efficiency and Mass for Turbulent and Laminar Fluid Flow with 1 mm Minimum Channel Height.

significant drop off with increased channel size. Turbulent flow, as a result, is able to achieve weights 3 to 4 kg lighter than the lightest laminar flow design with 3 mm channels. Depending on minimum achievable cooling channel size, turbulent flow may provide significant benefit for the cooling topology assumed in this paper.

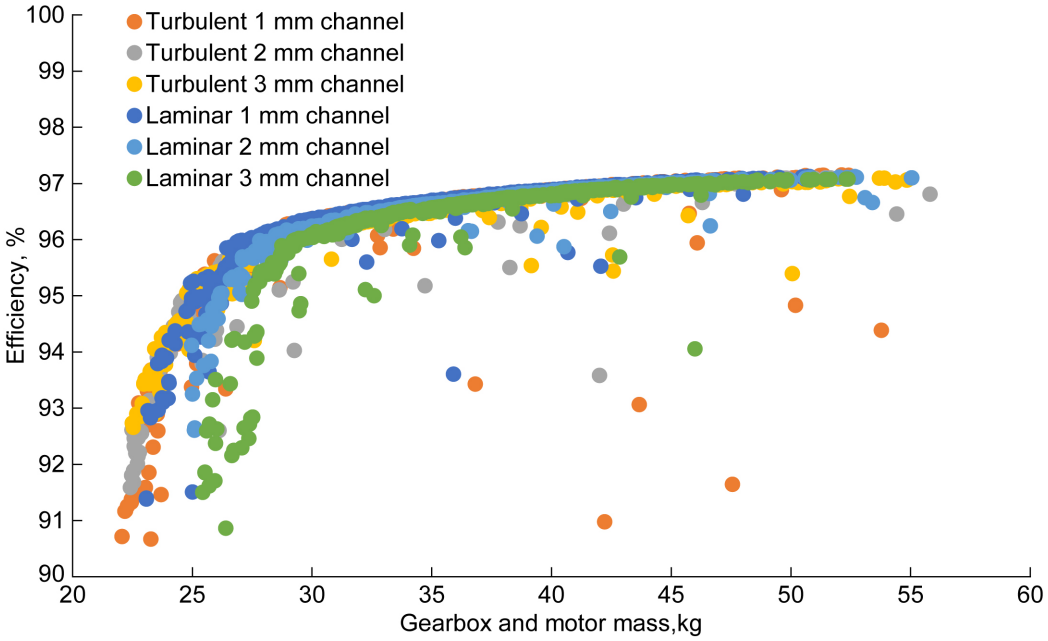


Figure 10.—Comparison of Efficiency and Mass for Turbulent and Laminar Fluid Flow with Varying Minimum Channel Height

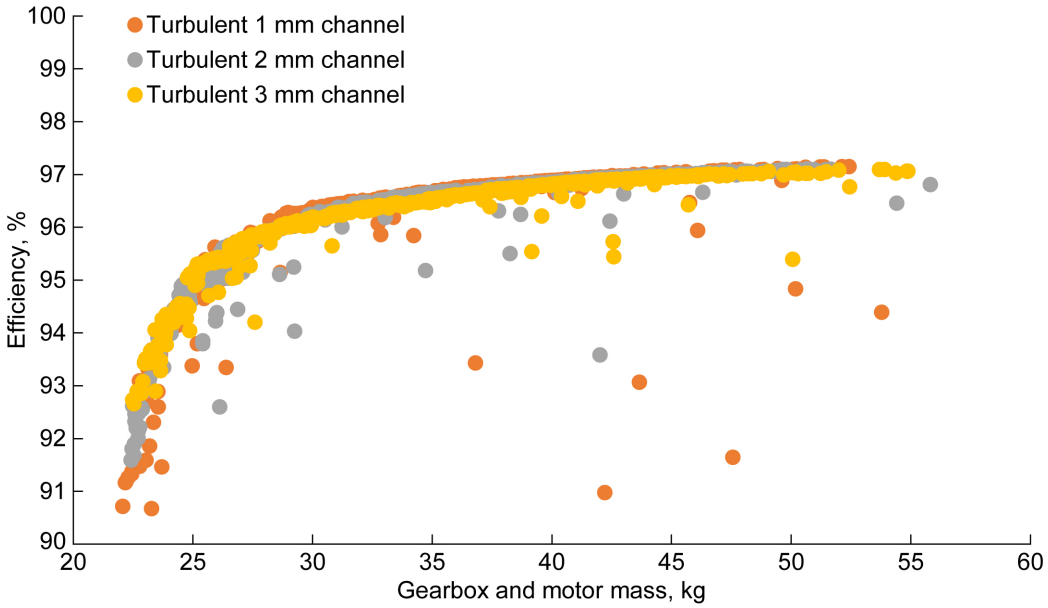


Figure 11.—Comparison of Efficiency and Mass for Turbulent Flow with Varying Minimum Channel Height.

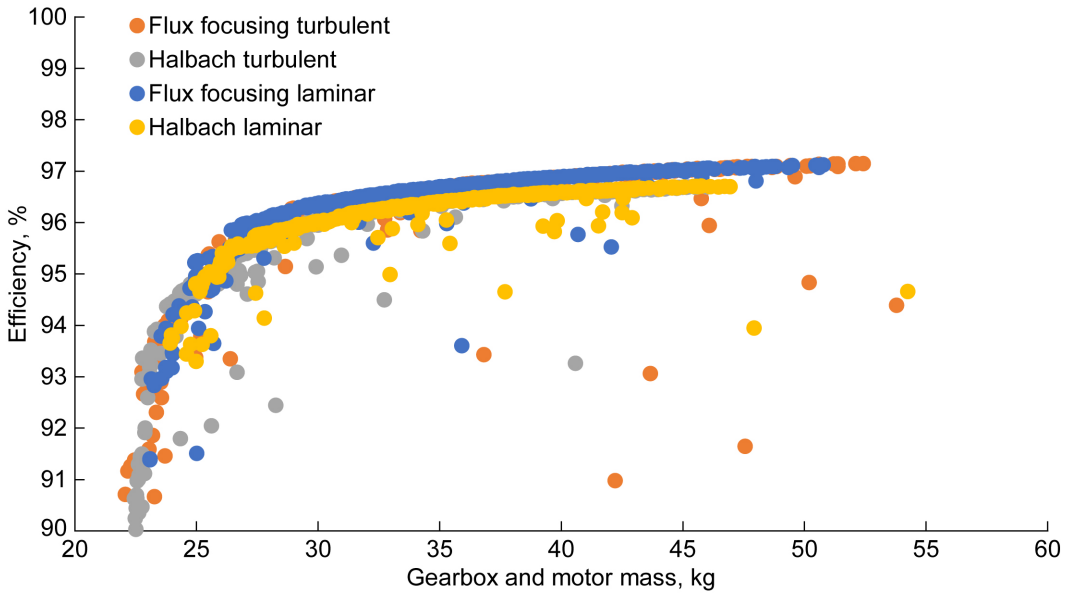


Figure 12.—Comparison of Efficiency and Mass between Halbach Array and Flux-Focusing Topologies.

### 3.4 Air Core Flux Focusing versus Halbach

For an initial comparison of the air-core flux-focusing technology to Halbach array motors, the design tool was modified for Halbach array rotors and run. To modify the code for Halbach motors, the rotor-produced magnetic field prediction was switched to the closed form solution for Halbach arrays from (Ref. 25). The rotor iron magnetic field variable was eliminated for the Halbach version of the design tool, otherwise all assumptions and variable ranges were maintained.

Figure 12 shows the comparison between flux focusing and Halbach arrays for both turbulent and laminar flow assuming a 1 mm minimum cooling channel height and carbon fiber shafting. Flux focusing motors are shown to be able to achieve higher efficiency than Halbach array motors at masses greater than ~28 kg. The Halbach array motors are shown to be able to achieve slightly smaller masses at lower efficiencies using turbulent cooling flows than the flux focusing topology. The margin of difference between the designs may however be within the error of the low fidelity design tool. Further higher fidelity modeling is needed to complete the comparison and will be the target of future work. However, the overall initial results show that the air-core flux focusing rotor topology is competitive with Halbach array motors.

## 4.0 Design Refinement

Based on the above results, a motor design with concentrated wound stator windings, laminar cooling flow, and a carbon fiber shaft was selected for further refinement. Table V gives the design tool output for the selected design. Even though the max electrical frequency was constrained to a maximum of 1,000 Hz, the design optimized to a slightly higher frequency. This is due to needing to separately calculate pole count and then recalculate electrical frequency in the design tool. The effects of the slight increase in frequency are negligible. The following sections cover preliminary FEA based magnetic, thermal, and mechanical modeling of the machine to raise the design fidelity.

TABLE V.—RESULTING VALUES FROM OPTIMIZATION OF EXAMPLE MOTOR

| | | | |
|---|---|---|---|
| Rotor rpm | 5035.3 | Rotor iron flux density | 1.3 T |
| Electrical frequency | 1007 Hz | Stator back iron flux density | 1.9 T |
| Rotor tip speed | 75.2 m/s | Stator tooth iron flux density | 2 T |
| Pole pairs | 12 | $B_{g1}$ | 0.935 T |
| Slots | 36 | RMS current per layer | 728 A |
| --- | --- | --- | --- |
| Stack length | 49.9 mm | Resistive loss | 1727.5 W |
| Stator inner radius | 144.3 mm | Stator iron loss | 1077 W |
| Stator outer radius | 164.3 mm | Magnet loss | 0 |
| Stator thickness | 20 mm | Rotor iron loss | 0 |
| Stator tooth width | 9.4 mm | Proximity loss | 0 |
| Stator back iron thickness | 4.9 mm | Windage loss | 120 W |
| Stator tooth tip thickness | 1.5 mm | Bearing loss | 23 W |
| Airgap | 1 mm | Flow loss | 7.62 W |
| Rotor hoop thickness | 0.625 mm | Motor efficiency | 97.13% |
| Rotor outer radius | 142.7 mm | --- | --- |
| Magnet thickness | 11.4 mm | Magnet mass | 2.5 kg |
| Magnet width | 23.1 mm | Rotor iron mass | 1.5 kg |
| Rotor iron pole percentage | 38% | Stator iron mass | 4.43 kg |
| --- | --- | Winding mass | 3.06 kg |
| Gearbox specific torque index | 0.9992 | Bobbin mass | 0.2 kg |
| Gearbox efficiency | 98.95% | Bearing mass | 0.058 kg |
| Gearbox mass | 13.67 kg | Housing mass | 2.13 kg |
| --- | --- | Shaft mass | 0.4 kg |
| Fluid flow rate | 18.6 L/min | EM mass | 11.51 kg |
| Fluid channel thickness | 1.2 mm | Mechanical mass | 2.59 kg |
| Fluid channel width | 14.1 mm | Motor mass | 14.1 kg |
| Flow velocity | 0.49 m/s | --- | --- |
| Flow Reynolds number | 258 | Total mass | 28 kg |
| Convection coefficient | 731 $W/m^2K$ | Max. winding temperature | 167.8 °C |
| Flow loss | 7.6 W | Efficiency | 96.09% |

## 4.1 Magnetic FEA Modeling

A magnetic model of the selected machine was created in FEA assuming a perfect sine stator current waveform. Pseudo time stepping analysis was first used to assess the average torque and magnetic loss in the machine. Subsequently transient analysis was used to assess the eddy current losses in the shaft for different shaft materials.

### 4.1.1 Pseudo Time Stepping Analysis

Pseudo time stepping analysis was used to both capture machine average torque and the magnetic field in the motor components relative to rotor position. The average torque from FEA was used to re-calculate required stator current and stator resistive losses. Magnetic field vs rotor position (Figure 13) was used to obtain a better estimate for stator iron loss and initial estimates for rotor magnetic losses and stator winding proximity losses using the method described in Reference 7. Iron losses were calculated using the improved generalized Steinmetz Equation (26). Magnet losses were calculated using the method described in Reference 27. A magnet lamination size of 2 mm was assumed. The stator proximity loss estimate was made for a winding wire diameter of 1 mm. Table VI provides a comparison of design tool and FEA predicted losses.

The design tool is shown to underpredict losses in the motor by approximately 10 percent. The dominant source of error in the loss prediction are in the stator current and stator iron loss. This underprediction is due to the motor design code neglecting the field produced by the stator current. Correspondingly the machine design has higher flux density in the stator iron than the tool predicts resulting in higher iron loss and the iron operating closer to saturation. The iron operating close to

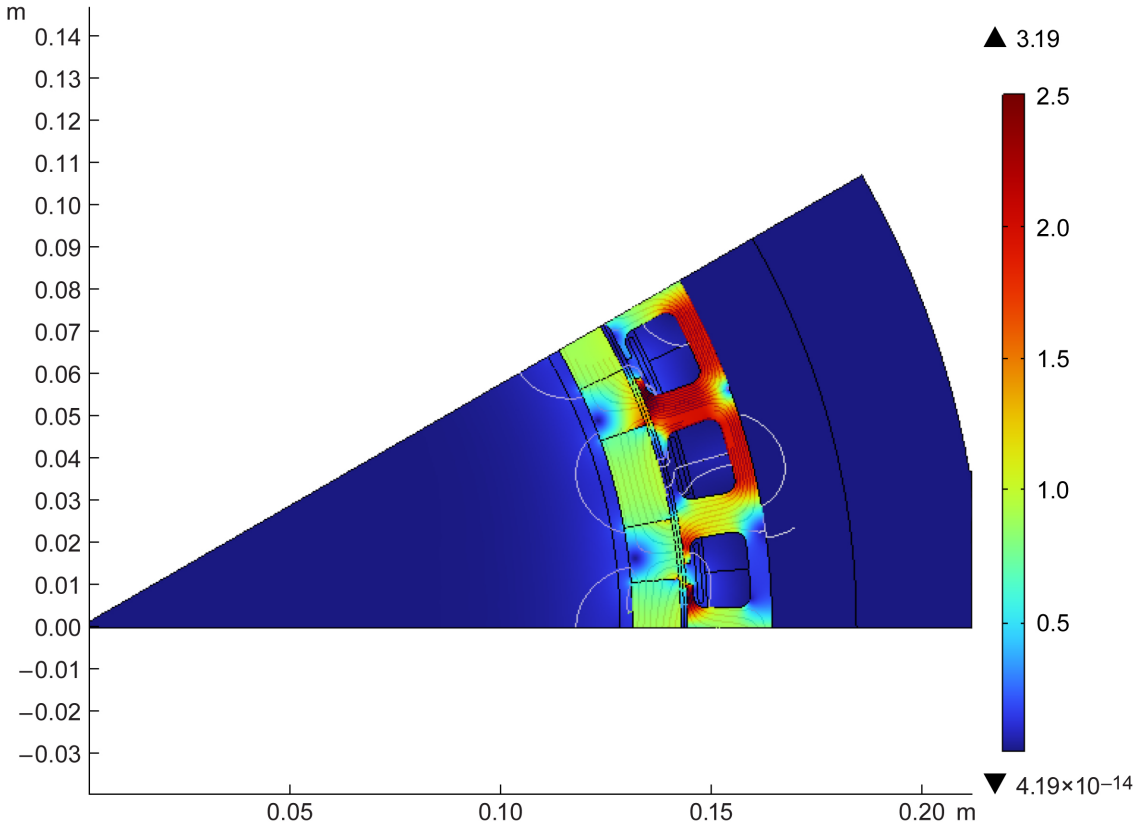


Figure 13.—Magnetic Flux Density in Chosen Flux-Focusing Design using Pseudo Time Stepping Analysis.

TABLE VI.—DESIGN TOOL AND FEA PREDICTED PERFORMANCE VALUES OF EXAMPLE MOTOR

| Output | Design code | FEA | Error, percent |
|---|---|---|---|
| RMS current per layer | 728 | 769 | –5.3 |
| Resistive loss | 1727.5 | 1884.938046 | –8.4 |
| Stator iron loss | 1077 | 1136 | –5.2 |
| Magnet loss | 0 | 29 | n/a |
| Rotor iron loss | 0 | 44 | n/a |
| Proximity loss | 0 | 50 | n/a |
| Windage loss | 120 | | n/a |
| Bearing loss | 23 | | n/a |
| Flow loss | 7.62 | | n/a |
| Total loss | 2955.12 | 3294.558046 | –10.3 |
| Efficiency | 0.971297008 | 0.968105212 | 0.3 |

saturation results in lower iron permeability and correspondingly more current being needed to produce the same torque. Increasing stator back iron thickness and tooth width each by 1 mm in a subsequent FEA analysis reduced iron saturation and reduced required current to a value close to what was predicted by the design tool. Future iterations of the design tool will either include calculations of the field resulting from stator current or add additional iron field margin.

### 4.1.2 Transient Shaft Eddy Current Analysis

In order to further explore whether carbon fiber shafting is required for the air core flux focusing rotor topology, transient FEA analysis of the machine design was carried out to obtain estimates for shaft eddy currents. Cases for aluminum, titanium, and 316 stainless metals being a 3 mm rim that supports the rotor magnetic components were run. Figure 14 shows the eddy current response for Aluminum and Ti materials at the same snapshot in time. Time average eddy current losses were taken for one electrical period of the machine. Losses were predicted to be 51 W for aluminum, 34 W for Ti, and 48 W for 316 stainless. These loss values would only amount to a less than 2 percent increase for the total losses of the machine and correspondingly would only effect efficiency by ~0.5 percent. They would however be a significant portion of the total losses on the machine's rotor. Carbon fiber losses values were not estimated here as the eddy current response of the material is not well defined. NASA plans to conduct eddy current loss experiments in the future to assess losses in carbon fiber hoops and shafts.

## 4.2 Thermal FEA

Thermal FEA analysis of the machine was carried out using both the loss results from the design tool and the loss results from the pseudo time stepping FEA. Only a 2D FEA model of the stator was used. As shown in Figure 15, in both cases, the FEA model predicted higher temperatures than the design tool. Both temperatures are, however, below 200 °C, providing sufficient margin for the end windings to be below the max use temperature of the motor winding insulation at 240 °C. Further refinement of the analytical thermal model is needed before the next iteration of design to correct for the error between its prediction and FEA.

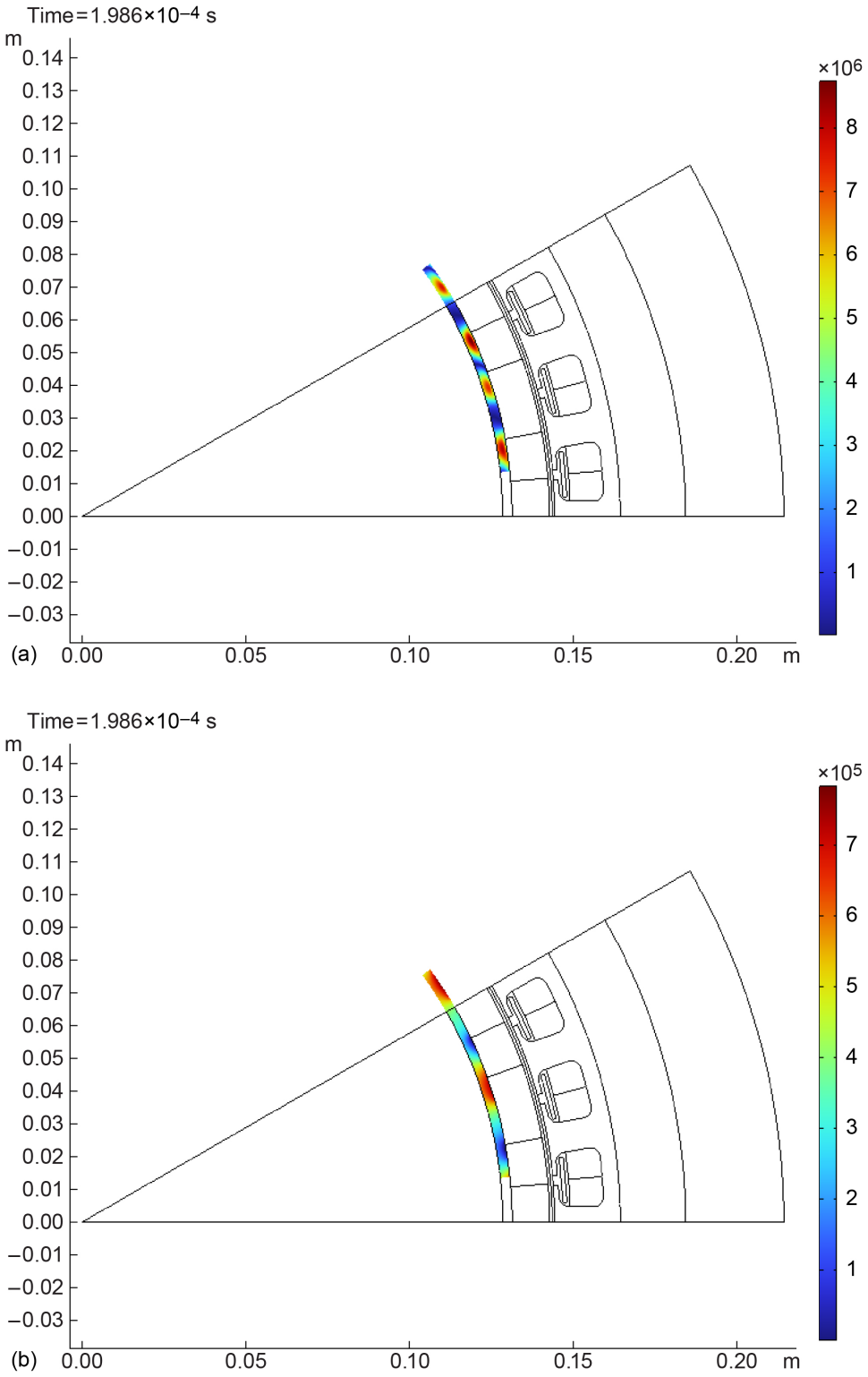


Figure 14.—Eddy Current Response for Chose Flux-Focusing Motor with Aluminum (a) and Titanium (b) Shafts.

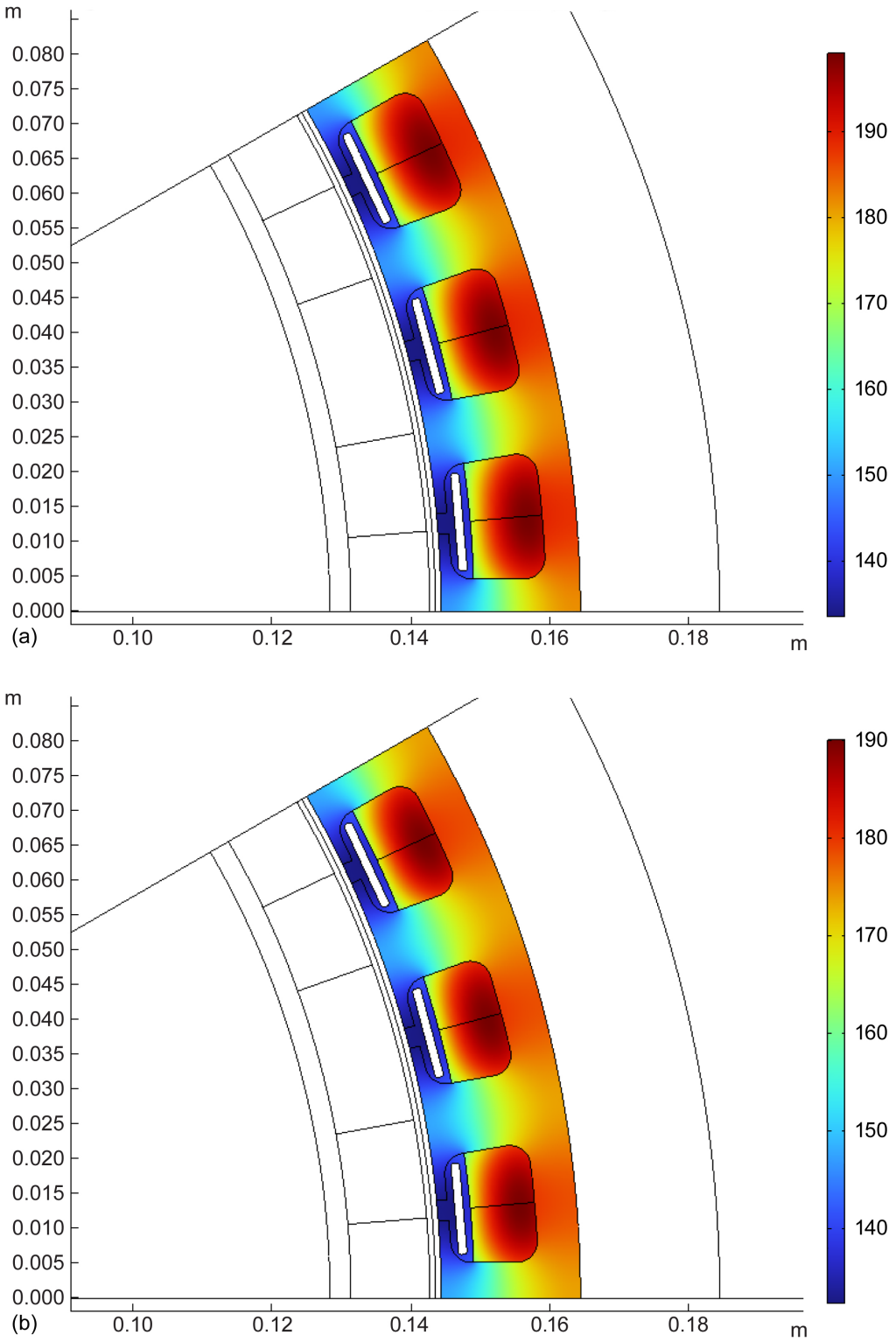


Figure 15.—FEA Predicted Stator Iron and Winding Temperatures Using Predicted Losses from Design Tool (a) and Pseudo Time Stepping Analysis (b).

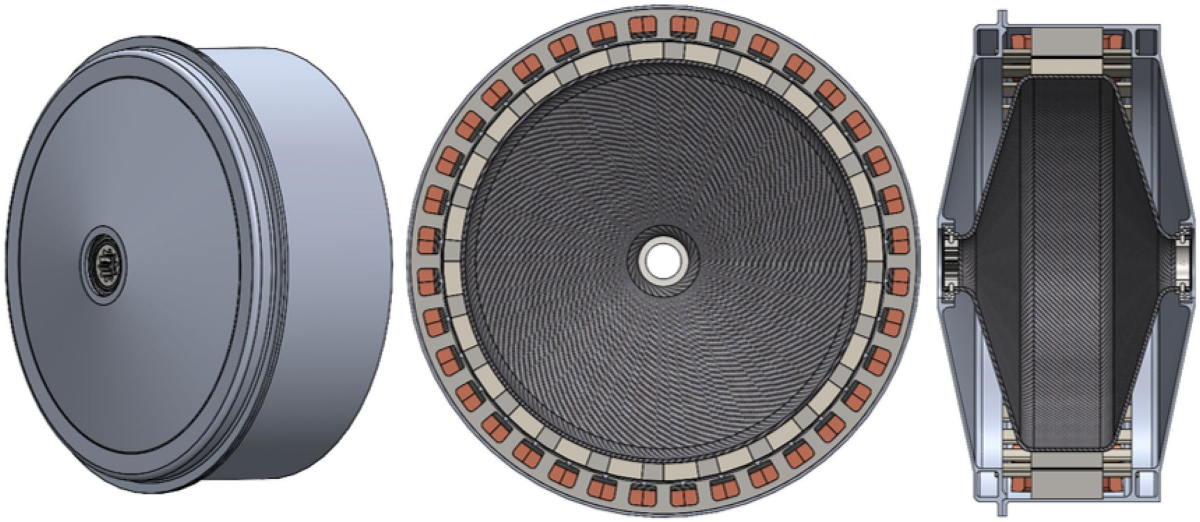

Figure 16.—Preliminary CAD of the Chosen Flux-Focusing Motor with Carbon Fiber Shaft.

## 4.3 Mechanical Modeling

Figure 16 shows preliminary CAD of the motor. Fasteners, current leads, fluid inlet/outlets, and connections to the gearbox/output shaft are neglected in this preliminary CAD. Machine weight in the CAD comes to 15.1 kg compared to 14.1 kg predicted by the design tool. The bulk of this error comes from the mass of the fluid manifold and added length of the cooling bobbins. Corrections for this weight error will be applied in the next iteration of the design tool. Assuming a 10 percent margin for the components neglected in this CAD iteration, the motor's estimated continuous specific power is ~6 kW/kg.

### 4.3.1 Mechanical Stress

FEA mechanical stress analysis was carried out in two models. The first model focused on the magnet retaining hoop stress. A $1/12^{th}$ circumferential section of the rotor geometry was used in order to allow for a detailed mesh in the retaining hoop to magnet interface. The model geometry and mesh are shown in Figure 17. Unidirectional carbon fiber properties are applied to the retaining hoop. Woven prepreg carbon fiber properties are applied to the shaft. Curvilinear coordinate systems are used to align the unidirectional properties in the hoop in the circumferential direction and the woven properties in the axial and circumferential direction in the shaft. The hoop is modeled with an interference fit to represent the pretension it would apply to the magnet assembly. Frictionless contact is used for the interface of the hoop to the magnet assembly to allow for the pretension analysis. Corresponding axial and tangential constraints are applied to the hoop geometry. All other contacts are modeled with bonded boundary conditions and a normal stiffness of 1E13 N/m representing a low bond stiffness for a 0.1 mm layer of epoxy.

The model is constrained with radial and axial constraints at both bearing locations. A torsional constraint is applied at the spline interface. Cyclic symmetry conditions were applied to the circumferential faces of all the components. Torque was applied to the outer radial face of the magnetic components and rotational velocity to 610 rad/s was applied. Figure 18 shows max principal stress results for both the hoop pretension step and the full rotational velocity of the rotor. High pretension is needed to eliminate the possibility of epoxy failure between the shaft and the rotor magnetic material under rotation. Peak hoop stress after rotation is shown to be lower than the design stress of 800 MPa as the bond between the shaft and the magnetic components as well as the bond between the magnetic components supports some of the centripetal loading.

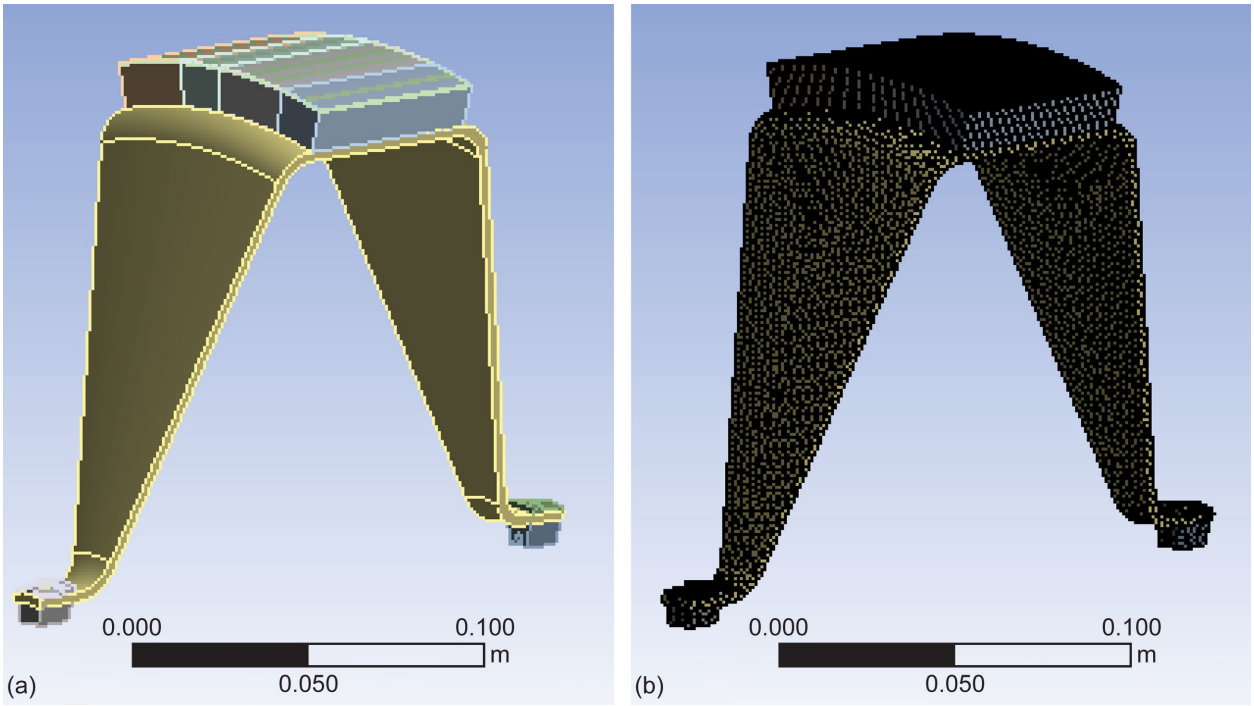


Figure 17.—Model Geometry and Mesh Used in Mechanical Hoop Stress Analysis.

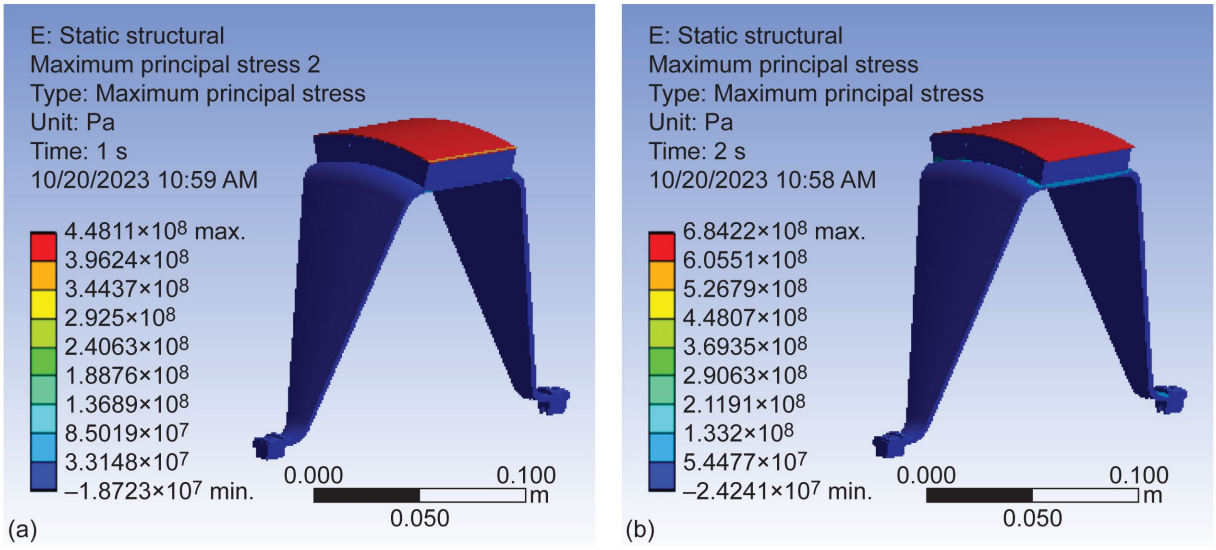


Figure 18.—Max Principal Stress Results for Hoop Pretension Step (a) and Full Rotational Velocity (b).

The second mechanical stress model focused on the shaft itself. The geometry and mesh for this model are depicted in Figure 19. No symmetry is used to allow the asymmetric loading resulting from the peak conditions in Table II to be applied to the model. All interfaces in this model were modeled as bonded with a 1E13 N/m normal stiffness. Bearings elements with radial stiffness of 4E8 N/m were used to constrain the model in the radial direction. Spring foundation elements were used to constrain the model axially.

Figure 20 shows the resulting stress in the shaft with full rotational velocity, full torque, and the peak loads resulting from the conditions in Table II. Relatively benign stress levels below 100 MPa are present well below the max allowable stress in the carbon fiber.

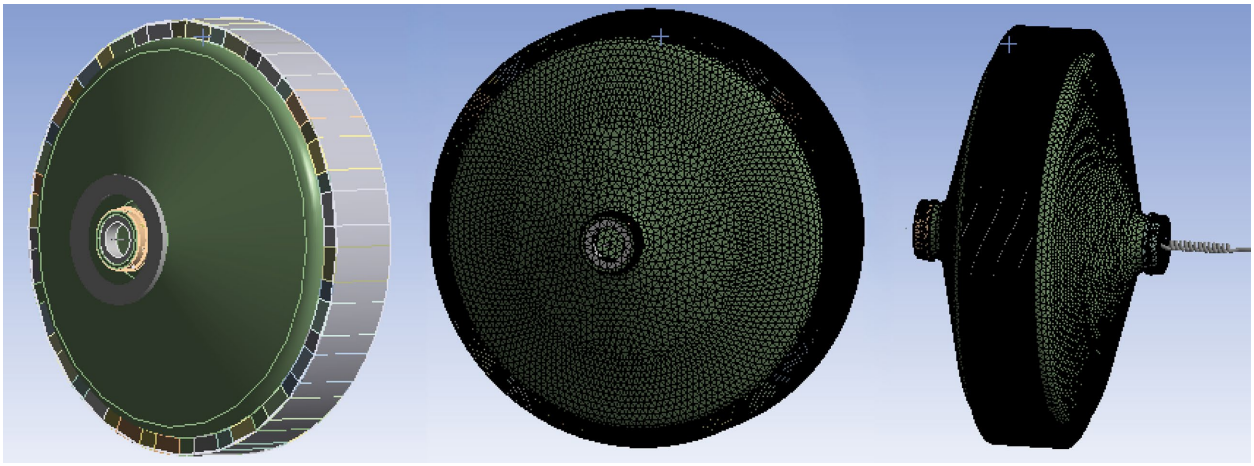

Figure 19.—Geometry and Mesh of Full Shaft and Rotor Used in Mechanical Hoop Stress Analysis.

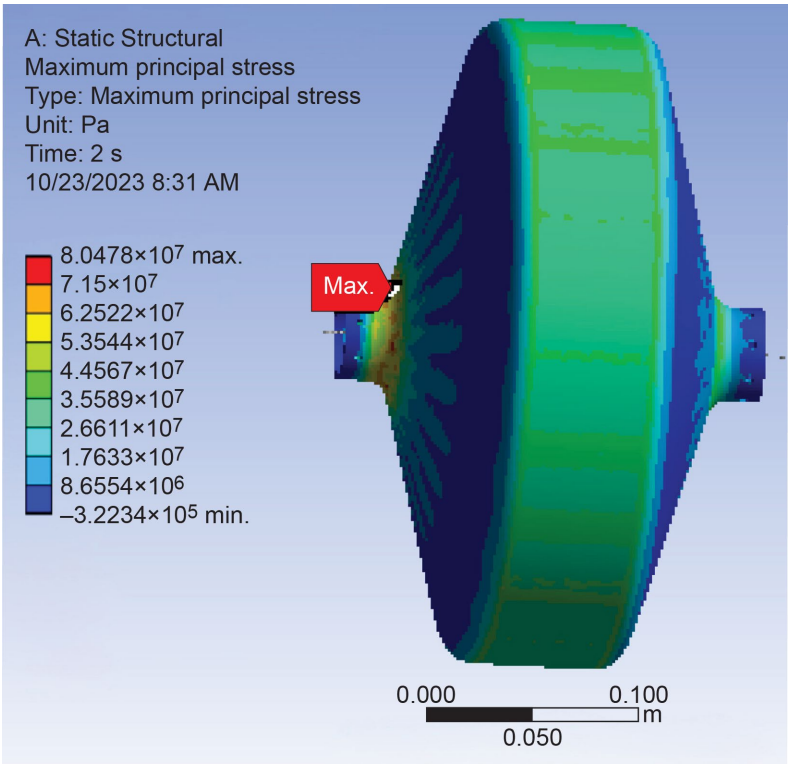


Figure 20.—Resulting Stresses in Shaft and Rotor at Full Rotational Velocity, Torque and Peak Loading.

### 4.3.2 Rotor Dynamics Analysis

Rotor dynamics analysis was completed using the same model of the rotor as was used for the shaft structural analysis. The Campbell diagram resulting from the rotor dynamics analysis of the rotor and shaft design is shown in Figure 21. Mode 1 in the diagram is a torsional mode outside of the operating regime of the machine but could possibly be excited by torque ripple at a given operating speed. Mode 3 (Figure 22) is the forward whirl of the first bending mode of the rotor, the mode that governs shaft critical speed and the mode the shaft was designed to suppress in the design tool. It is found to be closer to four times greater than the shaft nominal rotational speed (~84 Hz), which is well above the design target for the shaft of two times rotor speed. The discrepancy results from the shaft model in the design tool assuming a straight shaft slightly smaller than the bore diameter of the bearing. The steel bearing sleeves and magnetic components themselves may also increase the effective stiffness of the carbon fiber shaft, increasing the actual critical speed. Future work will try to refine the shaft model to create more accurate first bending mode and shaft mass predictions.

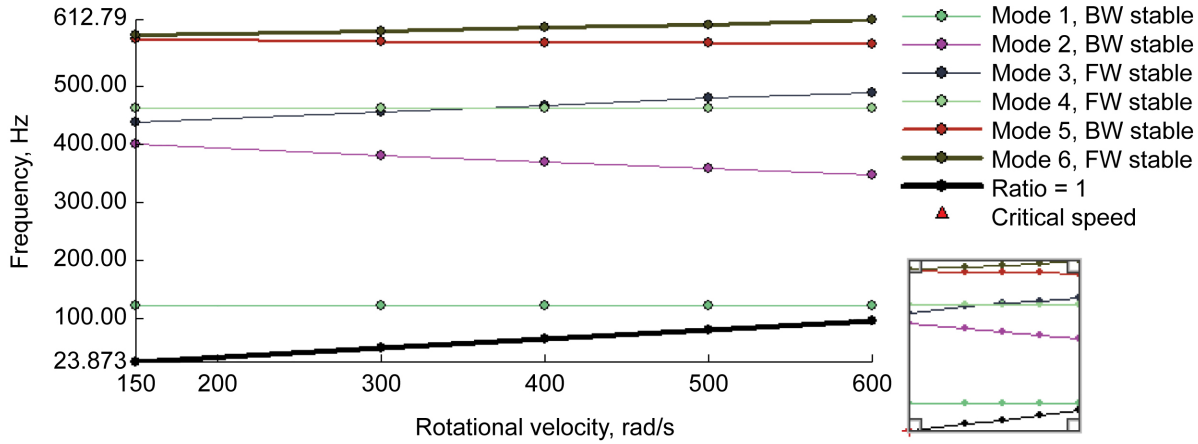


Figure 21.—Campbell Diagram from Analysis of Carbon Fiber Shaft.

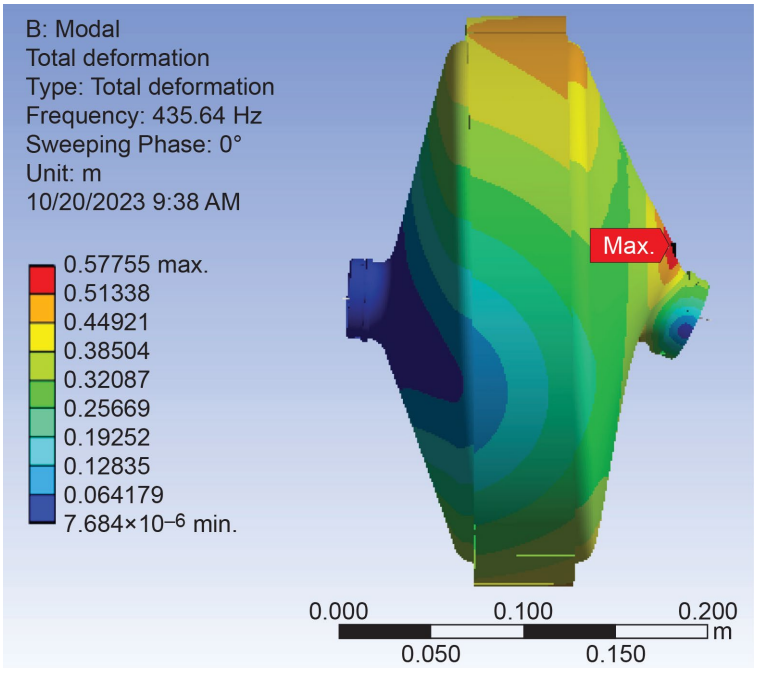


Figure 22.—Forward Whirl of First Bending Mode of Carbon Fiber Shaft and Rotor. Mode Number 3 in Figure 21.

# 5.0 Conclusions

This paper presents the design of an air-core flux focusing permanent magnet synchronous machine. A developed design tool for the machine topology was details. The design tool was used to study the design space for the machine topology. The design study results suggest that the machine topology can be competitive with Halbach array machined designs. A selected design was analyzed with high fidelity analysis and shown to be able to achieve close to 97 percent efficiency and 6 kW/kg. The higher fidelity analysis identified some areas of improvement for the design tool. Future work will implement improvements to the design tool and expand the design space to cover more complex cooling and rotor topologies. Additionally shaft prototyping will be used to refine the carbon fiber rotor shaft model and inform future iterations of carbon fiber shaft design for electric motors.

# Appendix A.—Thermal Network Model Equations

In the thermal reluctance network, the thermal resistance of solid components is estimated as

$$R = \frac{l}{kA} \tag{44}$$

where $l$ is the length of the element, $A$ is the perpendicular cross-sectional area of the element, and $k$ is the thermal conductivity of the element. For elements which pass through materials with varying thermal conductivities, the thermal reluctance becomes the sum of the individual reluctances of each material in the path such that

$$R = \frac{l_1}{k_1 A} + \frac{l_2}{k_2 A} + \frac{l_3}{k_3 A} + \cdots \tag{45}$$

where $l_x$ represents the length spanned by the material with conductivity $k_x$.

For liquid elements, the thermal resistance can be calculated using the formula

$$R = \frac{1}{hA} \tag{46}$$

where $h$ is the convection coefficient of the liquid and $A$ is contact area with the fluid. The convection coefficient is

$$h = \frac{\mathrm{Nu} * k}{\mathrm{HD}} \tag{47}$$

where Nu is the Nusselt Number of the flow, $k$ is the liquid's thermal conductivity, and HD is the hydraulic diameter of the flow channel. The hydraulic diameter can be calculated using

$$\mathrm{HD} = \frac{4A}{P} \tag{48}$$

Where $A$ is the cross sectional area of the duct and $P$ is the perimeter of the duct (Ref. 28). The Nusselt Number of the flow depends on the channel geometry and the Reynold's number of the flow. The Reynold's number of the flow measures the ratio between inertial and viscous forces in the flow. The Reynold's number can be calculated using the equation

$$\mathrm{Re} = \frac{v_{\mathrm{fluid}} * \mathrm{HD} * \rho_{\mathrm{fluid}}}{\mu_{\mathrm{fluid}}} \tag{49}$$

where $v_{\mathrm{fluid}}$ is the velocity of the flow, $\rho_{\mathrm{fluid}}$ is the density of the fluid, and $\mu_{\mathrm{fluid}}$ is the dynamic viscosity of the fluid (Ref. 28). Reynold's numbers less than 3000 is assumed to represent laminar flow in this paper while Reynold's numbers greater than 3000 are assumed to correspond to turbulent flow turbulent flow. For fully developed flow in aa rectangular cooling channel, the Nusselt number of the flow can be calculated using

$$\mathrm{Nu}=\begin{cases} 1.051\ln\left(\dfrac{b}{a}\right)+2.89,\ \mathrm{Re}<3000 \\ \dfrac{\left(\dfrac{f}{8}\right)(\mathrm{Re}-1000)\mathrm{Pr}}{1+12.7\left(\dfrac{f}{8}\right)^{\frac{1}{2}}\left(\mathrm{Pr}^{\frac{2}{3}}-1\right)},\ \mathrm{Re}\geq 3000 \end{cases} \tag{50}$$

where $b$ and $a$ are the dimensions of the channel with $b \geq a$, Pr is Prandtl Number and $f$ is the Moody friction factor (Ref. 28). The Moody friction factor also depends on the Reynold's number, and can be found using

$$f=\begin{cases} \dfrac{64}{\mathrm{Re}}, & \mathrm{Re}\geq 3000 \\ (0.79\ln(\mathrm{Re})-1.64)^{-2}, & \mathrm{Re}<3000 \end{cases} \tag{51}$$

The fluid will experience head loss as it flows through the channel, with the pressure drop being estimated in this paper as

$$\Delta P_{\mathrm{flow}}=\rho_{\mathrm{fluid}}\frac{(fv^2)}{2*\mathrm{HD}}L_{\mathrm{channel}} \tag{52}$$

where $\rho_{\mathrm{fluid}}$ is the fluid density, $v$ is the fluid velocity, and $L_{\mathrm{channel}}$ is the length of the flow channel. The required pumping power for the flow is calculated as

$$P_{\mathrm{loss,cooling}}=\Delta P_{\mathrm{flow}}\frac{\dot{m}}{\rho_{\mathrm{fluid}}} \tag{53}$$

where $\dot{m}$ is the mass flow of the fluid.

The thermal reluctance model can be solved as a system of linear equation solving the heat balance at each node such that

$$q_1=\frac{T_1-T_2}{R_{12}}+\frac{T_1-T_3}{R_{13}}\cdots \tag{54}$$

where $q_x$ is the heat load into node x, $T_x$ is the temperature of node x, $T_y$ is the temperature of node $y$, and $R_{xy}$ is the thermal resistance between nodes $x$ and $y$.

# References


1. J. Zhoa, X. Zhang, N. Swaminathan, and K.S. Haran, "An Overview of High Specific Power Electrical Machines and Drives Technologies for Electrified Aircraft," in IEEE Energy Conversion Congress and Exposition (ECCE), Detroit, MI, 2022. https://ieeexplore.ieee.org/document/9948102
2. T.P. Dever, K.P. Duffy, A.J. Provenza, PL. Loyselle, B.B. Choi, C.R. Morrison, Lowe and M. Angela, "Assessment of Technologies for Noncryogenic Hybrid Electric Propulsion," NASA, January 2015. https://ntrs.nasa.gov/citations/20150000747
3. J. Swanke, D. Bobba, T. Jahns, and B. Sarlioglu, "Comparison of Modular PM Propulsion Machines for High Power Density," IEEE Transportation Electrification Conference and Expo (ITEC), pp. 1–7, 2019. https://ieeexplore.ieee.org/document/8790587
4. T. Balachandran, J. Reband, M. Lewis, and K. S. Haran, "Co-Design of Integrated Propeller and Inner Rotor PMSM for Electric Aircraft Application," in 2021 IEEE International Electric Machines & Drives Conference (IEMDC), Hartford, CT, USA, 2021. https://ieeexplore.ieee.org/document/9449579
5. D. Lee and et al., "Design and Prototype of a High Power Density Slotless PMSM for Direct Drive Aircraft Propulsion," in 2021 IEEE Power and Energy Conference at Illinois (PECI), Urbana, IL, 2021. https://ieeexplore.ieee.org/document/9435256
6. W. Ouyang, K. Rhatigan, E. Pershouse, and D. Barone, "High Power Density Permanent Magnet Propulsion Motor Development for Urban Air Mobility Applications," in AIAA Scitech 2023 Forum, National Harbor, MD, 2023. https://arc.aiaa.org/doi/pdf/10.2514/6.2023-0673
7. T.F. Tallerico, "NASA Reference Motor Designs for Electric Vertical Takeoff and Landing Vehicles," in AIAA Propulsion and Energy 2021 Forum, Virtual, 2021. https://ieeexplore.ieee.org/document/9704824
8. T.F. Tallerico, A.D. Smith, J.T. Thompson, E.L. Pierson, C.A. Hilliker, D. Avanesian, W. Miller, and K.W. Monaghan, "Outer Mold Line Cooled Electric Motors for Electric Aircraft," in AIAA/IEEE Electric Aircraft Technologies Symposium, Virtual, 2020. https://ieeexplore.ieee.org/document/9235129
9. H. Anderson and et al., "Design and Manufacturing of a High-Specific-Power Electric Machine for Aircraft Propulsion," in AIAA AVIATION 2023 Forum, San Diego CA, 2023. https://arc.aiaa.org/doi/pdf/10.2514/6.2023-4158
10. A. Anderson, J. Gutknecht, and T. Tallerico, "Kokomo: An Electric Motor for a Rotating Cryocooler," in NASA Technical Memo, Cleveland Ohio, 2024.
11. T.F. Tallerico, "Genetic Optimization of Planetary Gearboxes Based on Analytical Gearing Equations," NASA TM-20220008843, Cleveland, 2022. https://ntrs.nasa.gov/citations/20220008843
12. T.F. Tallerico, J. Chapman, and A.D. Smith, "Preliminary Electric Motor Drivetrain Optimization Studies for Urban Air Mobility Vehicles," in AIAA/IEEE Electric Aircraft Technologies Symposium, Anaheim, 2022. https://ieeexplore.ieee.org/abstract/document/9813780
13. T.F. Tallerico, A.D. Anderson, M.G. Granger, and J.M. Gutnecht, "Analytical Design and Performance Estimation Methods for Aircraft Permanent Magnet Synchronous Machines," in NASA TM-20230010737, Cleveland, 2023. https://ntrs.nasa.gov/citations/20230010737
14. T.A. Lipo, Introduction to AC Machine Design, Piscataway: IEEE Press, 2018. https://ieeexplore.ieee.org/book/8068864
15. C.P. Steinmetz, "On the Law of Hysteresis," Transactions of the American Institute of Electrical Engineers, vol. 9, no. 1, pp. 1–64, 1892. https://ieeexplore.ieee.org/document/5570437
16. A. Hughes and B. Drury, Electric Motors and Drives, Waltham, MA: Elsevier Ltd, 2013.

17. T. Tallerico and A.D. Smith, “Combined Electromagnetic and Thermal Design Optimization Studies of in-Slot Cooling for UAM Electric Motors,” in IEEE Transportation Electrification Conference & Expo (ITEC), Anaheim, 2022. https://ieeexplore.ieee.org/document/9813967
18. SKF Group, “SKF Super Precision Bearing Catalog,” March 2016. [Online]. Available: https://www.skf.com/binaries/pub12/Images/0901d19680495562-Super-precision-bearings-catalogue---13383_2-EN_tcm_12-129877.pdf. [Accessed July 2020]. https://cdn.skfmediahub.skf.com/api/public/0901d19680495562/pdf_preview_medium/0901d19680495562_pdf_preview_medium.pdf
19. S. Dunkerley, “On the whirling and vibration of shafts,” Philosophical Transactions of the Royal Society of London, vol. 185, pp. 279–360, 1894. https://royalsocietypublishing.org/doi/10.1098/rsta.1894.0008
20. E. Oberg, F.D. Jones, H.L. Horton, and H.H. Ryffel, “Critical Speed Formulas,” in Machinery’s Handbook, South Norwalk Connecticut, Industrial Press, 2016, p. 190. https://search.worldcat.org/title/945663469
21. SKF Group, “SKF model for calculating the frictional moment,” [Online]. Available: https://www.skf.com/binary/12-299767/0901d1968065e9e7-The-SKF-model-for-calculating-the-frictional-movement_tcm_12-299767.pdf. [Accessed January 2020]. https://cdn.skfmediahub.skf.com/api/public/0901d1968065e9e7/pdf_preview_medium/0901d1968065e9e7_pdf_preview_medium.pdf
22. W. Johnson, C. Silva, and E. Solis, “Concept Vehicles for VTOL Air Taxi Operations,” in American Helicopter Society Technical Conference on Aeromechanics Design for Transformative Vertical Flight, San Francisco, 2018. https://ntrs.nasa.gov/citations/20180003381
23. C. Silva, W. Johnson, K. Antcliff, and P.D. Michael, “VTOL Urban Air Mobility Concept Vehicles for Technology Development,” in AIAA Aviation, Atlanta, 2018. https://arc.aiaa.org/doi/10.2514/6.2018-3847
24. T. Tallerico, J. Chapman, and A. Smith, “Design Studies on Mechanically Geared, Magnetically Geared, and Direct Drive Drivetrains for UAM Applications,” in AIAA AVIATION 2023 Forum, San Diego, 2023. https://arc.aiaa.org/doi/10.2514/6.2023-4506
25. Z.P. Xia, Z.Q. Zhu, and D. Howe, “Analytical Magnetic Field Analysis of Halbach Magnetized Permanent-Magnet Machines,” IEEE TRANSACTIONS ON MAGNETICS, vol. 40, no. 4, 2004. https://ieeexplore.ieee.org/document/1325354
26. V. Venkatachalam, C. Sullivan, T. Abdallah, and H. Tacca, “Accurate Prediction of Ferrite Core Loss with Non-Sinusoidal Waveforms Using only Steinmetz Parameters,” in Computers in Power Electronics, Mayaguez, 2002. https://ieeexplore.ieee.org/document/1196712
27. S. Ruoho, T. Santa-Nokki, J. Kolehmainen, and A. Arkkio, “Modeling Magnet Length in 2-D Finite Element Analysis of Electric Machines,” IEE Transactions on Magnetics, vol. 45, no. 8, 2009. https://ieeexplore.ieee.org/document/5170208
28. T.L. Bergman, A.S. Lavine, F.P. Incropera, and D.P. Dewitt, Introduction to Heat Transfer, Hoboken: John Wiley & Sons, 2011. https://books.google.com/books?id=YBaNaLurTD4C&printsec=frontcover&source=gbs_ViewAPI#v=onepage&q&f=false
29. W. Sixel, M. Liu, G. Nellis, and B. Sarliogle, “Ceramic 3-D Printed Direct Winding Heat Exchangers for Thermal Management of Concentrated Winding Electric Machines,” IEEE Transactions on Industry Applications, vol. 57, no. 6, pp. 5829–5840, 2021. https://ieeexplore.ieee.org/document/9511846